



Modeling mercury isotopic fractionation in the atmosphere[☆]

Zhengcheng Song^a, Ruoyu Sun^b, Yanxu Zhang^{a,*}

^a School of Atmospheric Sciences, Nanjing University, Nanjing, 210023, China

^b Institute of Surface-Earth System Science, School of Earth System Science, Tianjin University, 300072, Tianjin, China

ARTICLE INFO

Keywords:

Mercury isotope
Isotope model
GEOS-Chem
Total gaseous mercury

ABSTRACT

Mercury (Hg) stable isotope analysis has become a powerful tool to identify Hg sources and to understand its biogeochemical processes. However, it is challenging to link the observed Hg isotope fractionation to its global cycling. Here, we integrate source Hg isotope signatures and process-based Hg isotope fractionation into a three-dimensional isotope model based on the GEOS-Chem model platform. Our simulated isotope compositions of total gaseous Hg (TGM) are broadly comparable with available observations across global regions. The isotope compositions of global TGM, potentially distinguishable over different regions, are caused by the atmospheric mixture of anthropogenic, natural, and re-emitted Hg sources, superimposed with competing processes, notably gaseous Hg(0) dry deposition and Hg redox transformations. We find that Hg(0) dry deposition has a great impact on the isotope compositions of global TGM and drives the seasonal variation of $\delta^{202}\text{Hg}$ in forest-covered regions. The atmospheric photo-reduction of Hg(II) dominates over Hg(0) oxidation in driving the global $\Delta^{199}\text{Hg}$ (and $\Delta^{201}\text{Hg}$) distribution patterns in TGM. We suggest that the magnitude of isotope fractionation associated with atmospheric aqueous-phase Hg(II) reduction is likely close to aquatic Hg(II) reduction. Our model provides a vital tool for coupling the global atmospheric Hg cycle and its isotope fractionation at various scales and advances our understanding of atmospheric Hg transfer and transformation mechanisms.

1. Introduction

Mercury (Hg) in the atmosphere derives from both natural processes (e.g., direct emission from volcanic eruption and re-emission from ocean evasion, 6500–8200 Mg yr⁻¹) and anthropogenic activities (e.g., coal burning and gold mining, 1900–2900 Mg yr⁻¹) (Driscoll et al., 2013; Selin et al., 2008). Atmospheric Hg is mainly in the form of gaseous elemental Hg(0) with varying proportions as gaseous reactive Hg(II)_g and particle-bound Hg(II)_p [sum of Hg(II)] (Streets et al., 2017; Zhang et al., 2015; Saiz-Lopez et al., 2020). The Hg redox chemistry has undergone a rapid development in recent years (e.g., Saiz-Lopez et al., 2020; Shah et al., 2021; Horowitz et al., 2017; Ariya et al., 2004). The Hg(0) can reside in the air for several months, allowing for global transport (Zhang et al., 2016; Li et al., 2020b; Selin et al., 2007), while it can also be oxidized to Hg(II) by halogen atoms (e.g., Br and Cl). The Hg(II) is water-soluble and can be efficiently removed from the air by wet and dry deposition (Gencarelli et al., 2017; Pacyna et al., 2016; Horowitz et al., 2017; Saiz-Lopez et al., 2018). Together with Hg(0) dry deposition, these processes are the major sinks of atmospheric Hg. The

deposited Hg can be partly reduced and released back to the atmosphere from the earth's surface, comprising a complex global biogeochemical Hg cycle. Meanwhile, terrestrial and aquatic Hg(II) can be transformed into methylmercury, a neurotoxicant that is readily bioaccumulated and biomagnified within food webs (Sun et al., 2020; Wu et al., 2020).

Mercury has seven stable isotopes (196, 198, 199, 200, 201, 202, and 204amu.), which undergo mass-dependent fractionation (MDF; reported as $\delta^{202}\text{Hg}$) and mass-independent fractionation (MIF; reported as $\Delta^{\text{xxx}}\text{Hg}$ where xxx is 199, 200, 201, or 204) (Blum and Bergquist, 2007). The MDF is ubiquitous in nearly all physical, chemical, and biological processes (Blum et al., 2014), while large odd mass number isotope MIF (odd-MIF: $\Delta^{199}\text{Hg}$ and $\Delta^{201}\text{Hg}$) predominantly takes place in abiotic and photochemical Hg transformations (Zheng and Hintelmann, 2010; Blum and Bergquist, 2007; Blum et al., 2014; Sherman et al., 2010). The even mass number isotope MIF (even-MIF: $\Delta^{200}\text{Hg}$ and $\Delta^{204}\text{Hg}$) that is mainly observed in atmospheric samples is suspected to be triggered by photochemical reactions of Hg in the upper atmosphere (Chen et al., 2012; Blum and Johnson, 2017).

The multidimensional fractionation system of Hg isotopes has been

[☆] This paper has been recommended for acceptance by Wen-Xiong Wang.

* Corresponding author.

E-mail address: zhangyx@nju.edu.cn (Y. Zhang).

widely used for the evaluation of atmospheric Hg sources and biogeochemical processes. Typically, end-member mixing models are used to assess atmospheric Hg sources, considering that the anthropogenic, re-emitted, and natural Hg sources are potentially distinguishable in their Hg isotope compositions (Kwon et al., 2020; Fu et al., 2021b; Sherman et al., 2010). For example, seasonal isotope variation of total gaseous Hg [TGM≡Hg(0) + Hg(II)_g] in the western Antarctic is affected by the inland wind and sea-ice dynamics in austral winter and summer, respectively (Yu et al., 2021). Hg(0) isotope composition in the Pyrenees is thought to be a mixture of European anthropogenic emissions and Atlantic Ocean re-emissions (Fu et al., 2016). Atmospheric Hg in a coastal urban-industrial region (Florida, USA) is discerned as a combination of local anthropogenic emissions, marine-influenced sources, and continental sources (Demers et al., 2015).

While mixing models are useful, they assume simple mass conservation in a steady-state with little consideration of the changes of isotope fractionation of Hg from sources to receptors. Laboratory and observational studies have proved that atmospheric processes can reshape the atmospheric Hg isotope compositions, such as Hg(0) oxidation by halogen atoms (Sun et al., 2016a) and Hg(0) uptake by vegetation (Zhou et al., 2021; Demers et al., 2013). Numerical simulations of Hg isotopes provide an efficient tool to interpret observations with detailed source isotope signatures and isotope fractionation dynamics. In previous studies, Sonke (2011) integrated Hg odd-MIF in a fully-coupled box model and revealed the multiplicity of photochemical odd-MIF in aerosol, soil, snow, and vegetation surface. Later, Sun et al. (2019) expanded this Hg isotope box model by implementing source Hg isotope signatures and all three Hg isotope fractionation (i.e., MDF, odd-MIF, and even-MIF) pathways, aiming to reproduce Hg isotope distribution in Earth surface reservoirs. Although these box model studies could simulate global Hg isotope distribution, the box models are based on highly simplified physical-chemical frameworks without accounting for the spatial heterogeneity of the source Hg emissions and biogeochemical processes determining Hg transport and transformation.

In this study, spatially-resolved atmospheric source Hg isotope signatures and isotopic fractionation processes are integrated into a state-of-the-art Euler-based three-dimensional atmospheric transport model (GEOS-Chem) (Zhang et al., 2016; Horowitz et al., 2017; Holmes et al., 2010). The objectives of this study are threefold: i) to develop a three-dimensional atmospheric model that simulates the fractionation of individual Hg isotopes; ii) to simulate the distribution of Hg isotope compositions in the global atmosphere and its connection with source mixture and underlying physiochemical processes; and iii) to examine if Hg isotope observations in the atmosphere can be reproduced using current knowledge on the atmospheric Hg cycle and Hg isotope fractionation. We also discuss the implications of our results on Hg cycling and potentially the health effects (Zhang et al., 2021).

2. Methodology

2.1. Model description

The GEOS-Chem model (Version 12.5.0) is used for the simulation of atmospheric Hg stable isotopes. In the model, atmosphere transport is driven by GEOS-FP assimilated meteorological data from the NASA Global Modeling and Assimilation Office (GMAO). The simulation is conducted with 4°latitudes × 5°longitudes horizontal resolution and 47 vertical layers extending to the mesosphere. The model uses a scheme for Planetary Boundary Layer (PBL) mixing following Lin and McElroy (2010). Dry deposition of Hg is applied to Hg(0), Hg(II)_g, and Hg(II)_p above both land and ocean surfaces, which includes Hg(II)_g deposition by sea salt aerosols uptake throughout the marine boundary layer (MBL) (Zhang et al., 2019; Holmes et al., 2009). Dry deposition velocity in the model is calculated based on the resistance-in-series scheme, which depends on the land type and leaf area index (LAI) (Wesely, 1989; Jacob et al., 1992; Jacob and Wofsy, 1990). Wet deposition is applied to Hg

(II)_g and Hg(II)_p, but not to Hg(0) because of its low Henry's Law constant. The simulation of wet deposition includes rainout and washout from large-scale and convective precipitation (Amos et al., 2013; Horowitz et al., 2017).

The Hg(0)/Hg(II)_g redox chemistry follows Horowitz et al. (2017), which suggests that atomic bromine (Br) of the marine organobromine origin is the main atmospheric Hg(0) oxidant and that second-stage oxidation of HgBr is mainly by NO₂ and HO₂ radicals. The formed Hg(II)_g can be absorbed by aerosols to form Hg(II)_p, and the partitioning coefficient is temperature dependent, following Amos et al. (2012). The monthly mean concentrations of these oxidants and aerosol mass are taken from previously archived GEOS-Chem simulations (Schmidt et al., 2016). We consider all seven stable Hg isotopes: ¹⁹⁶Hg, ¹⁹⁸Hg, ¹⁹⁹Hg, ²⁰⁰Hg, ²⁰¹Hg, ²⁰²Hg, and ²⁰⁴Hg for Hg(0), Hg(II)_g, and Hg(II)_p, which results in a total of 21 advected tracers. We conduct a 3-y simulation for 2014–2016. The first 2 years are used for initialization, and the third year is used for result analysis.

2.2. Isotope notation

We use δ^{xxx}Hg notations to express the simulated and measured Hg isotope compositions of atmospheric Hg species. These notations are defined as the isotope ratio difference between simulated or measured atmospheric Hg species and the NIST-3133 standard in a unit of permil (‰):

$$\delta^{xxx}\text{Hg} (\text{‰}) = [({}^{xxx}/198\text{Hg})/({}^{xxx}/198\text{Hg}_{\text{NIST3133}}) - 1] \times 1000 \quad (1)$$

MIF is calculated as below:

$$\Delta^{199}\text{Hg} = \delta^{199}\text{Hg} - \delta^{202}\text{Hg} \times 0.252 \quad (2)$$

$$\Delta^{200}\text{Hg} = \delta^{200}\text{Hg} - \delta^{202}\text{Hg} \times 0.502 \quad (3)$$

$$\Delta^{201}\text{Hg} = \delta^{201}\text{Hg} - \delta^{202}\text{Hg} \times 0.752 \quad (4)$$

$$\Delta^{204}\text{Hg} = \delta^{204}\text{Hg} - \delta^{202}\text{Hg} \times 1.493 \quad (5)$$

The ^{xxx}/¹⁹⁸Hg_{NIST3133} in Eq (1) is treated as a constant, calculated using the relative Hg atomic abundances in NIST-3133 standard (Blum and Bergquist, 2007; Blum, 2012), namely ¹⁹⁶Hg = 0.155%, ¹⁹⁸Hg = 10.04%, ¹⁹⁹Hg = 16.94%, ²⁰⁰Hg = 23.14%, ²⁰¹Hg = 13.17%, ²⁰²Hg = 29.73%, and ²⁰⁴Hg = 6.83%.

2.3. Isotope chemistry

Biogeochemical transfer and transformation of Hg in the model are assumed to be accompanied by the kinetic Hg isotope fractionation where individual isotopes have slightly different rate coefficients. We compile all the Hg chemical reactions into the Kinetic Pre-Processor (KPP) that has been customized for the GEOS-Chem model. The rate coefficients (k_{xxx} for ¹⁹⁶Hg, ¹⁹⁸Hg, ¹⁹⁹Hg, ²⁰⁰Hg, ²⁰¹Hg, ²⁰²Hg, ²⁰⁴Hg) are derived from the experimental or modeled fractionation factors (α^{xxx}Hg, product/reactant) in various processes. The ¹⁹⁸Hg is taken as the reference isotope, and the k_{xxx} values of other isotopes are calculated as the product of the reference isotope rate coefficient and fractionation factors (α^{xxx}Hg, defined as the ratio of ^{xxx}/¹⁹⁸Hg for the product over reactant):

$$k_{xxx} = k_{198} \times \alpha^{xxx}\text{Hg} \quad (6)$$

The reported α^{xxx}Hg values obey the MDF kinetic law for MDF processes (Young et al., 2002; Sun et al., 2019; Sun et al., 2016a; Yang and Liu, 2015):

$$\ln(\alpha^{xxx}\text{Hg}) = \beta_{xxx} \times \ln(\alpha^{202}\text{Hg}) \quad (7)$$

where β is the scaling factor and is defined as below according to the transition state theory:

$$\beta_{xxx} = \ln(m_{198}/m_{xxx})/\ln(m_{198}/m_{202}) \quad (8)$$

where m is the mass of each isotope. We take β values as -0.507 , 0.252 , 0.502 , 0.752 , and 1.493 for ^{196}Hg , ^{199}Hg , ^{200}Hg , ^{201}Hg , ^{202}Hg , and ^{204}Hg , respectively, following Blum and Bergquist. (2007).

The total $\alpha^{xxx}\text{Hg}_{\text{TOT}}$ values can be deconvoluted as the product of the α values of MDF and MIF:

$$\alpha^{xxx}\text{Hg}_{\text{TOT}} = \alpha^{xxx}\text{Hg}_{\text{MDF}} \times \alpha^{xxx}\text{Hg}_{\text{odd-MIF}}, \text{ for } ^{199}\text{Hg} \text{ and } ^{201}\text{Hg} \quad (9)$$

$$\alpha^{xxx}\text{Hg}_{\text{TOT}} = \alpha^{xxx}\text{Hg}_{\text{MDF}} \times \alpha^{xxx}\text{Hg}_{\text{even-MIF}}, \text{ for } ^{200}\text{Hg} \text{ and } ^{204}\text{Hg} \quad (10)$$

The atmospheric kinetic isotope fractionation processes contained in the model are Hg(0) oxidation by Cl ($\alpha_{202}\text{MDFHg} = 0.99941$, $\alpha_{199}\text{MIFHg} = 0.99963$, $\alpha_{200}\text{MIFHg} = 1.00006$) (Sun et al., 2016a) and Br ($\alpha_{202}\text{MDFHg} = 0.99915$, $\alpha_{199}\text{MIFHg} = 0.99976$) (Sun et al., 2019; Sun et al., 2016a), as well as photo-reduction of Hg(II) ($\alpha_{202}\text{MDFHg} = 0.99894$, $\alpha_{199}\text{MIFHg} = 0.99783$) (Sun et al., 2019). A recent study (Shah et al., 2021) has presented a new chemistry mechanism that contains Hg oxidation by O_3/OH , gas-phase photoreduction of Hg(I) and Hg(II), etc. However, kinetic isotope effects are still unknown for these processes. Our model is thus considered as a “bulk” one for the isotope fractionation during redox chemistry, and the results are relatively robust as we simulate comparable gross flux of redox transformation with Shah et al. (2021). (Fig. 1, specific details are in the SI Text). The model also contained isotope fractionation during Hg(0) dry deposition, which is applied to Hg(0) dry deposition on land. Vegetation uptake of Hg(0), which is the dominant dry deposition pathway over the terrestrial surface (Jiskra et al., 2018), causes a significant MDF with an estimated enrichment factor ($\epsilon^{202}\text{Hg}$) varying from -1% to -4% (Jiskra et al., 2019; Enrico et al., 2016; Demers et al., 2013). The $\epsilon^{xxx}\text{Hg}$ is defined in relation to $\alpha^{xxx}\text{Hg}$ as follows:

$$\ln(\alpha^{xxx}\text{Hg}) = \epsilon^{xxx}\text{Hg}(\text{‰}) / 1000 \quad (11)$$

Snowpack uptake of Hg(0) can also induce a similar MDF as vegetation uptake, which is probably related to oxidation by halogens in the snow (Douglas and Blum, 2019). We assume a median value of $\epsilon_{202}\text{MDF} = -3\%$ for Hg(0) dry deposition to all land surfaces. The Hg deposited to land can be re-emitted to the atmosphere with reported $\epsilon^{199}\text{Hg}$ values ranging from 0.2% (vegetation effect) (Yuan et al., 2019; Hintelmann and Zheng, 2011) to 1.0% (terrestrial environment) (Zheng and Hintelmann, 2010; Sun et al., 2019), which contributes a relatively positive $\Delta^{199}\text{Hg}$ to Hg(0) in the air (Demers et al., 2013; Zheng and Hintelmann, 2010; Sherman et al., 2010). In addition, Henry’s Law

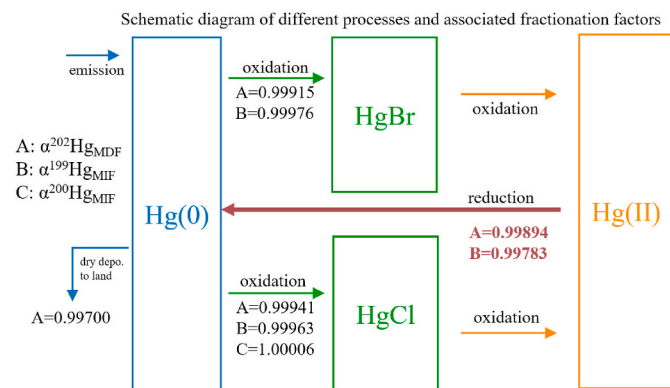


Fig. 1. Schematic diagram of different processes and associated fractionation factors (product/reactant). The $\alpha^{202}\text{Hg}_{\text{MDF}}$ for first-stage oxidation by Br is cited from Sun et al. (2019), which is a model evaluation, and the rest of $\alpha^{202}\text{Hg}_{\text{MDF}}$ and $\alpha^{xxx}\text{Hg}_{\text{MIF}}$ in oxidation are cited from Sun et al. (2016a) (details in SI). Fractionation factors for aqueous Hg photo-reduction are synthesized in Sun et al. (2019), and we utilized the average values. Factors for Hg(0) dry deposition through vegetation are cited from the median level of reported studies (Jiskra et al., 2019; Enrico et al., 2016; Demers et al., 2013). The $\alpha^{xxx}\text{Hg}_{\text{TOT}}$ are listed in Table A1.

constants for different isotopes are applied for Hg(II) wet deposition based on $\Delta m/m^2$ values for equilibrium MDF (Koster van Groos et al., 2014; Schauble, 2007). The fractionation factors are assumed to be constant due to the lack of experimental data, but all the redox chemistry rates are temperature-dependent following Horowitz et al. (2017), which allows isotope fractionation indirectly linked to temperature.

2.4. Isotope emissions

We use the EDGARv4.tox2 inventory for anthropogenic Hg emissions in the GEOS-Chem model (Muntean et al., 2018). This inventory has a global emission of 1800 tons Hg in 2010, and we scale this budget to 2100 tons according to the WHET inventory (Zhang et al., 2016). The EDGARv4.tox2 is based on IEA (2014) energy statistics, which include Hg released from various sectors and regions with a high resolution of $0.1^\circ \times 0.1^\circ$. Eleven sectors are included in the inventory, with the largest contribution from power generation (780 Mg y^{-1}), followed by artisanal and small-scale gold mining (ASGM, 665 Mg y^{-1}), cement production (180 Mg y^{-1}), non-ferrous industry (80 Mg y^{-1}), and others (480 Mg y^{-1}) (Muntean et al., 2018). Due to the scarcity of reported Hg isotope data for these sectors, we group these sectors into six categories, each with distinct isotope emissions (Table A2). Three different forms of Hg are distinguished, namely Hg(0), Hg(II)_g, and Hg(II)_p. Natural emissions include biomass burning (240 Mg y^{-1}) and geogenic emissions (200 Mg y^{-1}) (Zhang et al., 2016). Re-emissions from the ocean (3900 Mg y^{-1}), soil (690 Mg y^{-1}), and snow (90 Mg y^{-1}) are taken from recent modeling results (Zhang et al., 2016).

The isotopic compositions of different anthropogenic emission sources are synthesized in Sun et al. (2016b) and the total emissions are displayed in Fig. 2 (Fig. A1 for each sector). We assume that all Hg species emitted from anthropogenic source sectors conserve the Hg isotope compositions of their corresponding source materials following Sun et al. (2016b). One exception is the coal combustion sector. We adopt a shift of $+1.1\%$, $+0.05\%$, and -0.50% for $\delta^{202}\text{Hg}$ of the emitted Hg(0), Hg(II)_g, and Hg(II)_p, respectively, relative to the feed coal following Sun et al. (2014). Emissions from coal combustion and non-ferrous metal sectors are specified with distinct Hg isotope compositions in different regions because of the large Hg isotope variations across worldwide coal deposits and metal-ores (Fig. A1) (Sun et al., 2016b). The Hg isotope signatures from Chinese cement production sectors are extrapolated to the globe as China is the leading emitter for this sector (Fig. A1) (Li et al., 2021; Sun et al., 2016b). The intentional Hg use sectors (e.g., ASGM, Chlor-alkali industry, Hg cell technology, solid waste incineration, and agricultural waste burning) use liquid Hg for amalgamation reaction, then all the liquid Hg will volatilize to air through high-temperature heating. Thus, these emissions are estimated to conserve the isotopic composition of liquid Hg (Fig. A1) (Sun et al., 2016b). All the $\Delta^{200}\text{Hg}$ values emitted from anthropogenic sources are set to zero (Sun et al., 2016b).

The isotopic compositions of natural emissions are compiled from available observations, as shown in Table 1. Ocean emission has the largest flux with the $\delta^{202}\text{Hg}$ of $-0.21 \pm 0.39\%$, $\Delta^{199}\text{Hg}$ of $-0.25 \pm 0.09\%$, and $\Delta^{200}\text{Hg}$ of $-0.11 \pm 0.04\%$. Soil emission has the second flux with a negative $\delta^{202}\text{Hg}$ of $-1.90 \pm 1.04\%$ and a positive $\Delta^{199}\text{Hg}$ of $0.71 \pm 0.94\%$. Other emissions (e.g., biomass burning, geogenic emission) have relatively lower fluxes that exert an insignificant impact on the isotope composition of global TGM. The specific information about selecting these sources is interpreted in SI text, and the model utilizes the mean values.

3. Results and discussion

3.1. Model evaluation

Fig. 3 shows the simulated annual mean TGM concentrations in the surface air as the sum of all the seven isotope concentrations. We

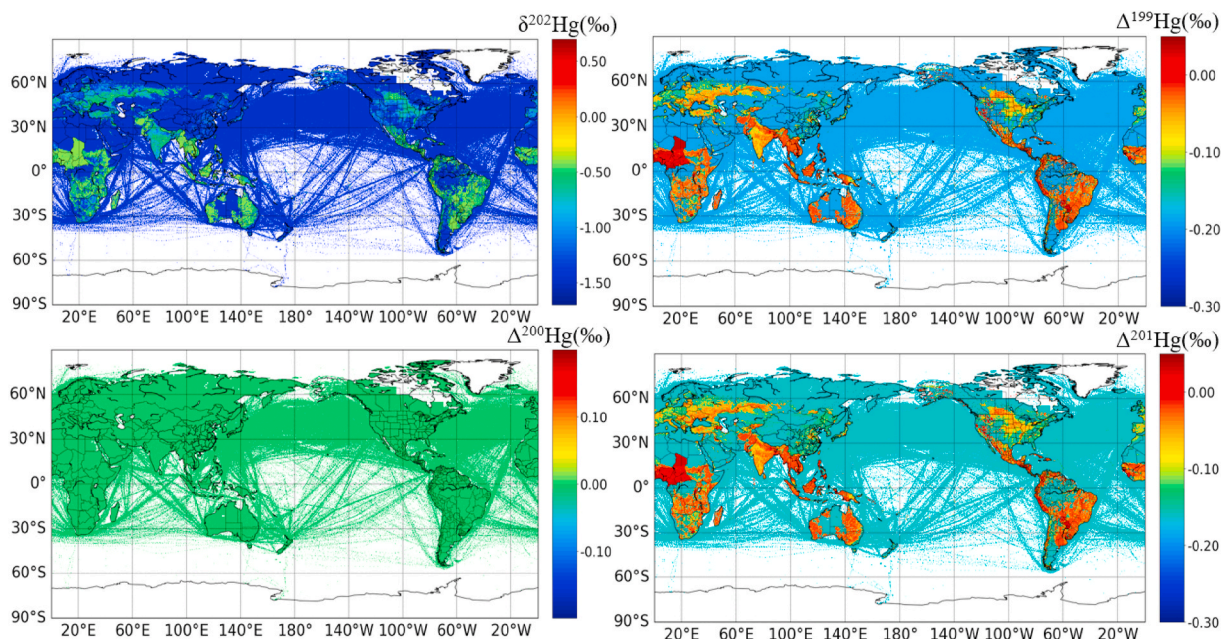


Fig. 2. Isotopic compositions of Hg as released from all the anthropogenic emissions.

Table 1

Isotope composition of Hg end-members emitted from natural and re-emission sources.

Sources	$\delta^{202}\text{Hg}$ (‰)	SD	$\Delta^{199}\text{Hg}$ (‰)	SD	$\Delta^{200}\text{Hg}$ (‰)	SD	References
Soil (690 Mg y ⁻¹)	-1.90	1.04	0.71	0.94	0.10	0.00	(Fu et al., 2021b; Sun et al., 2019; Fu et al., 2018; Sonke, 2011)
Snow (90 Mg y ⁻¹)	0.74	0.13	-0.53	0.09	-0.07	0.02	Jiskra et al. (2019)
Ocean (3900 Mg y ⁻¹)	-0.21	0.39	-0.25	0.09	-0.11	0.04	(Fu et al., 2018; Rolison et al., 2013)
Geogenic (200 Mg y ⁻¹)	-0.76	0.22	0.05	0.06	0.03	0.05	Sun et al. (2016b)
Biomass burning (240 Mg y ⁻¹)	1.39	1.59	-0.21	0.02	-0.11	0.00	(Kurz et al., 2020; Fu et al., 2018)

Note: The $\Delta^{201}\text{Hg}$ was calculated from $\Delta^{199}\text{Hg}/\Delta^{201}\text{Hg} \sim 1.2$, due to the absent data in references (1.2 was assumed from natural samples that plot within analytical uncertainty of the bounding $\Delta^{199}\text{Hg}/\Delta^{201}\text{Hg}$ ratios of 1.00 and 1.36) (Blum et al., 2014). All the $\Delta^{204}\text{Hg}$ was calculated from $\Delta^{200}\text{Hg}/\Delta^{204}\text{Hg} = -0.5$ (Blum and Johnson, 2017).

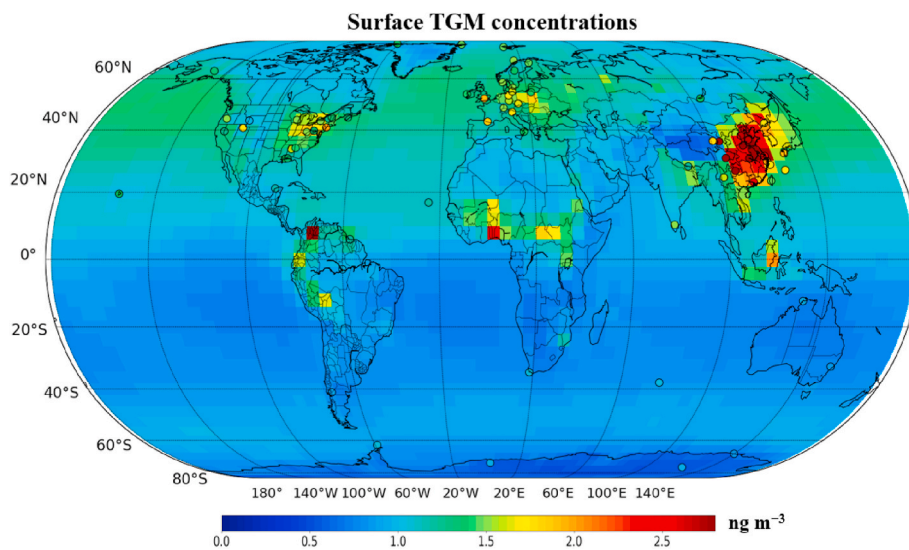


Fig. 3. Global distribution of total gaseous mercury (TGM) concentrations in surface air in units of ng m⁻³ (Background color: model results for 2016; Circles: observations during 2009–2018). Observations are annual mean compiled from Zhang et al. (2016) and Kwon et al. (2020), and those from Jiskra et al. (2019), Yu et al. (2020), Kurz et al. (2020), Nguyen et al. (2021), Fu et al. (2021b) and Yu et al. (2021).

compare the simulated results to the measured TGM data from literatures for 2009–2018, which contain 76 sites on both land and ocean surface. The modeled data (1.40 ± 0.49 ng m⁻³, n = 76) agrees well

with the observations (1.65 ± 0.67 ng m⁻³, n = 76), with a spatial correlation coefficient of 0.54. The model successfully reproduces the global patterns of observed TGM, showing higher concentrations in the

North Hemisphere (NH, $0.57\text{--}3.26\text{ ng m}^{-3}$) than in the Southern Hemisphere (SH, $0.51\text{--}2.01\text{ ng m}^{-3}$), and the highest concentrations in East Asia ($0.98\text{--}3.26\text{ ng m}^{-3}$). The model also captures well the high TGM sites in East Asia, Europe, and North America (Fig. 3). The modeled mean global TGM is comparable with the results simulated by Selin et al. (2007) ($1.63 \pm 0.10\text{ ng m}^{-3}$) and Horowitz et al. (2017) ($1.44 \pm 0.25\text{ ng m}^{-3}$). This indicates the reliable performance of our Hg isotope model.

3.2. Hg isotope compositions of simulated and observed TGM

We compute the isotope compositions ($\delta^{202}\text{Hg}$, $\Delta^{199}\text{Hg}$, $\Delta^{200}\text{Hg}$, and $\Delta^{201}\text{Hg}$) of the simulated TGM (Fig. 4). The simulated MDF ($\delta^{202}\text{Hg}$) is generally positive with a global range from -0.39‰ to 0.90‰ (min to

max, the same hereinafter) and higher at the poles ($0.60 \pm 0.15\text{‰}$) than in other regions ($0.29 \pm 0.09\text{‰}$). Regions with higher primary anthropogenic emissions are simulated to have lower $\delta^{202}\text{Hg}$ values [e.g., East Asia ($0.18 \pm 0.12\text{‰}$)] than regions with lower anthropogenic emissions (e.g., $\sim 0.60\text{‰}$ in Wisconsin forest of the U.S.) on land. Lower $\delta^{202}\text{Hg}$ values in Central Africa and South America are affected by the ASGM emission, which is the dominant Hg source in these areas (Muntean et al., 2018) and is characterized by negative $\delta^{202}\text{Hg}$ values (Fig. A1) (Sun et al., 2016b). The distribution pattern can also reflect the perturbation of atmospheric $\delta^{202}\text{Hg}$ by redox chemistry processes. Ocean re-emission is known to be the dominant Hg source for the SH due to the large ocean surface area (Horowitz et al., 2017; Li et al., 2020b; Bieser et al., 2020; Huang and Zhang, 2021). In the model,

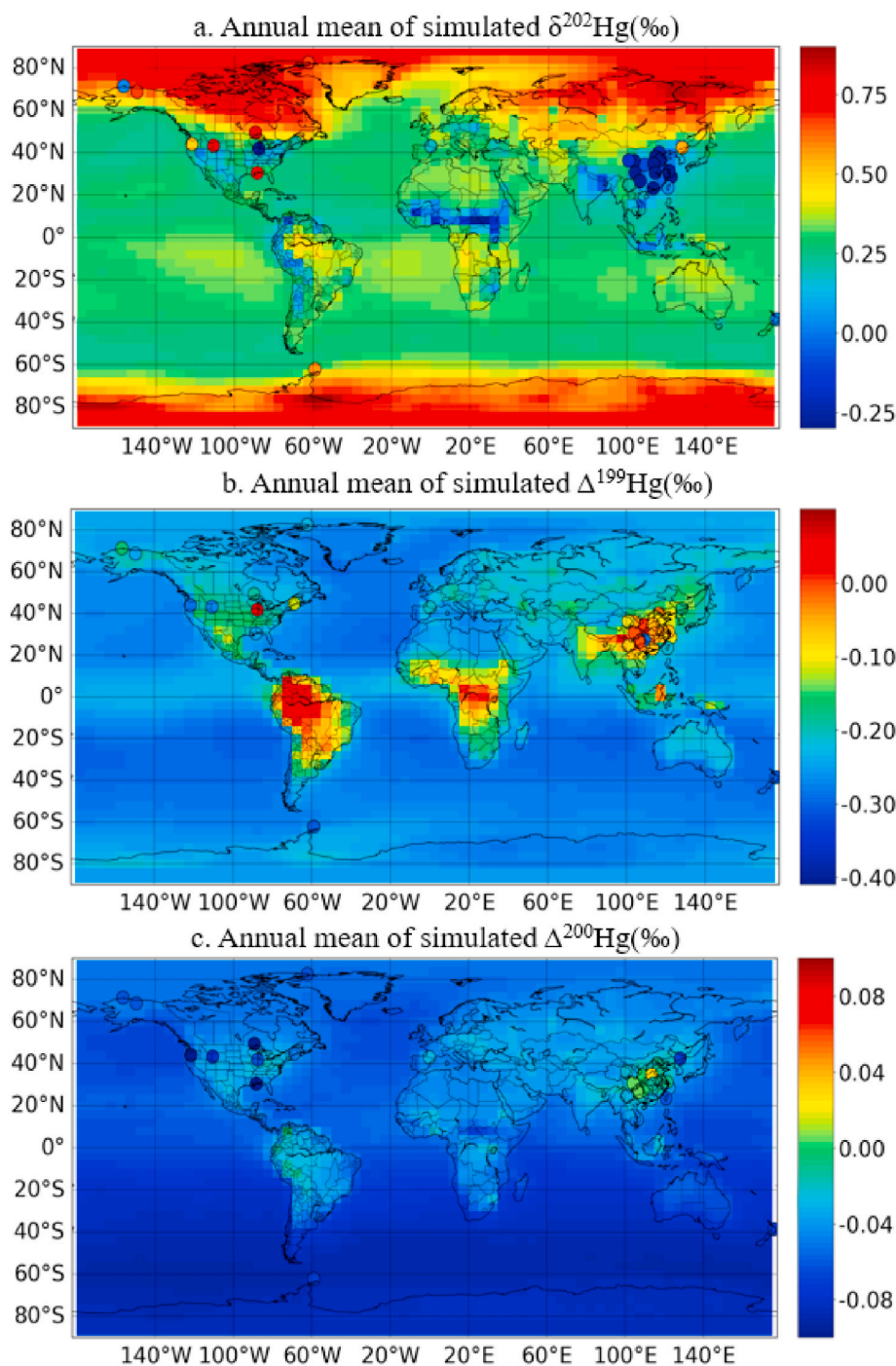


Fig. 4. Global distribution of the simulated annual mean of (a) $\delta^{202}\text{Hg}$, (b) $\Delta^{199}\text{Hg}$, and (c) $\Delta^{200}\text{Hg}$, of TGM in ground surface air. The observational data are from references (Xu et al., 2017; Yu et al., 2016; Fu et al., 2016; Yin et al., 2013; Rolison et al., 2013; Demers et al., 2013; Sherman et al., 2010; Gratz et al., 2010; Zheng et al., 2021; Yu et al., 2021; Nguyen et al., 2021; Fu et al., 2021b; Yu et al., 2020; Kurz et al., 2020; Jiskra et al., 2019; Fu et al., 2019; Obrist et al., 2017; Si et al., 2020; Demers et al., 2015).

ocean-emitted Hg(0) has a negative $\delta^{202}\text{Hg}$ (-0.21‰) (Table 1), whereas the $\delta^{202}\text{Hg}$ values above the NH sea surface all display positive values, which are mainly driven by the Hg(0) oxidation that enriches heavy isotopes in the reactant Hg(0) (Sun et al., 2019; Sun et al., 2016a).

We also synthesize available observations for $\delta^{202}\text{Hg}$ in the surface air in recent years (Fig. 4a). The observations generally remain sparse and mainly clustered in overpopulated NH regions (e.g., East Asia and North America) but not over the open oceans. Observed $\delta^{202}\text{Hg}$ of surface TGM exhibits negative values in regions with high anthropogenic emissions, such as East Asia ($-0.57 \pm 0.38\text{‰}$) (Fu et al., 2021b), and more negative values in Hg mining ($-2.15 \pm 0.09\text{‰}$) (Yin et al., 2013). TGM in forest areas generally shows positive $\delta^{202}\text{Hg}$ values (Fu et al., 2018; Yu et al., 2016; Enrico et al., 2016). In addition, observations in both the Arctic and the Antarctic all display positive $\delta^{202}\text{Hg}$ values in TGM (Jiskra et al., 2019; Douglas and Blum, 2019; Yu et al., 2021; Obrist et al., 2017). Our modeled $\delta^{202}\text{Hg}$ values are generally comparable to global distribution patterns of observed $\delta^{202}\text{Hg}$ (Fig. 4a). However, the modeled $\delta^{202}\text{Hg}$ values ($0.06 \pm 0.09\text{‰}$) are higher than observations ($-0.57 \pm 0.38\text{‰}$, $n = 10$) in Chinese urban areas, and are lower than observations in vegetation-covered areas of China and North America (e.g., $0.47 \pm 0.20\text{‰}$ at Mount Bachelor) (Kurz et al., 2020).

We speculate that the discrepancy between modeled and observed $\delta^{202}\text{Hg}$ suggests that the dry deposition process in the model cannot capture the vegetation-uptake isotope effect well in some areas. Vegetation uptake plays a key role in the global Hg cycle (Wang et al., 2020; Wang et al., 2019; Zhou et al., 2021; Jiskra et al., 2018), which pumps approximately 1310–1570 Mg of Hg(0) from the atmosphere per year (Zhou et al., 2021), accounting for 60–70% of anthropogenic emissions at present-day. Due to the strong preference for light isotope uptake, very high MDF has been reported during the vegetation-air exchange (Obrist et al., 2017; Demers et al., 2013; Demers et al., 2015). In the model, dry deposition velocity depends on LAI and the same isotope fractionation ($\epsilon_{MDF}^{202/198} = -3\text{‰}$) representing the vegetation uptake mechanism is applied to all the Hg(0) dry deposition on land (Fig. 1). The coarse resolution of the model cannot resolve the fine model grids with mixed urban and forest land types. Thus, the simulated $\delta^{202}\text{Hg}$ values of TGM in urban areas are higher than observations. The underestimated $\delta^{202}\text{Hg}$ at forest-covered sites (e.g., Camp Davis, USA) might be caused by the underestimation of vegetation uptake enrichment factors ($\epsilon_{MDF}^{202/198} \text{ plant-air}$), which are quite variable between -1‰ and -4‰ (Jiskra et al., 2019; Enrico et al., 2016; Demers et al., 2013). In addition, the underestimation of Hg(0) loading in the global forest as suggested by recent studies might be an alternative cause for this underestimation of $\delta^{202}\text{Hg}$ in TGM (Zhou et al., 2021; Obrist et al., 2021), which merits further examination in our future studies.

The model simulates higher odd-MIF ($\Delta^{199}\text{Hg}$) values over land surface ($-0.21 \pm 0.06\text{‰}$) than over the ocean ($-0.27 \pm 0.02\text{‰}$) (Fig. 4b). Higher values ($\sim 0\text{‰}$) are also modeled for regions with higher anthropogenic emissions (e.g., East Asia). This pattern largely reflects that of emissions: oceanic re-emissions typically have more negative $\Delta^{199}\text{Hg}$ (-0.41‰ to -0.03‰) (Rolison et al., 2013), anthropogenic sources are characterized by near-zero $\Delta^{199}\text{Hg}$, the land re-emissions have less negative but more variable $\Delta^{199}\text{Hg}$ (-0.32‰ – 0.71‰) (Table 1). The observed odd-MIF values are higher ($\sim 0\text{‰}$) over regions with higher anthropogenic emissions, while the coastal (e.g., Grand Bay, -0.25‰ of $\Delta^{199}\text{Hg}$) and mountain areas (e.g., Ailao, -0.10‰ of $\Delta^{199}\text{Hg}$) all display negative values. The modeled global means of $\Delta^{199}\text{Hg}$ ($-0.14 \pm 0.08\text{‰}$) and $\Delta^{201}\text{Hg}$ ($-0.12 \pm 0.07\text{‰}$) are generally comparable with the observations ($\Delta^{199}\text{Hg}$: $-0.12 \pm 0.09\text{‰}$; $\Delta^{201}\text{Hg}$: $-0.11 \pm 0.08\text{‰}$) with R^2 values of 0.55 ($n = 32$) and 0.36 ($n = 29$), respectively. The model also simulates odd-MIF values ($\Delta^{199}\text{Hg}$: $-0.10 \pm 0.06\text{‰}$, $\Delta^{201}\text{Hg}$: $-0.08 \pm 0.06\text{‰}$) consistent with observations in China, where the most measurements are available ($\Delta^{199}\text{Hg}$: $-0.08 \pm 0.06\text{‰}$, $\Delta^{201}\text{Hg}$: $-0.08 \pm 0.05\text{‰}$, $n = 19$). Comparable odd-MIF ($\Delta^{199}\text{Hg}$: $-0.21 \pm 0.02\text{‰}$, $\Delta^{201}\text{Hg}$: $-0.17 \pm 0.02\text{‰}$) are also

simulated in North America relative to observations ($\Delta^{199}\text{Hg}$: $-0.18 \pm 0.12\text{‰}$, $\Delta^{201}\text{Hg}$: $-0.15 \pm 0.09\text{‰}$, $n = 6$).

The modeled even-MIF ($\Delta^{200}\text{Hg}$) in TGM (Fig. 4c) has higher values over land ($-0.05 \pm 0.02\text{‰}$) than ocean ($-0.07 \pm 0.01\text{‰}$), and higher values in NH ($-0.05 \pm 0.01\text{‰}$) than in SH ($-0.08 \pm 0.01\text{‰}$). Observed $\Delta^{200}\text{Hg}$ displays higher values in East Asia than in North America, and the lowest values in polar regions. The simulated $\Delta^{200}\text{Hg}$ ($-0.03 \pm 0.02\text{‰}$) is well correlated with global observation ($-0.04 \pm 0.03\text{‰}$, $R^2 = 0.47$, $n = 32$), but is slightly overestimated over North America. The simulated pattern is mainly a consequence of the source mixture because only the Cl-oxidation has a minuscule fractionation factor (1.00006) for even-MIF in our model.

3.3. Polar regions

The polar regions have a unique atmospheric Hg chemistry characterized by Hg depletion events and active exchange of air with snow/ice (Ariya et al., 2004; Schroeder et al., 1998). Our model simulates positive $\delta^{202}\text{Hg}$ ($0.72 \pm 0.01\text{‰}$, $n = 3$), negative $\Delta^{199}\text{Hg}$ ($-0.24 \pm 0.01\text{‰}$, $n = 3$), and negative $\Delta^{200}\text{Hg}$ ($-0.05 \pm 0.00\text{‰}$, $n = 3$) in the Arctic ($>60^\circ\text{N}$), almost consistent with limited observations ($\delta^{202}\text{Hg}$: $0.45 \pm 0.30\text{‰}$, $\Delta^{199}\text{Hg}$: $-0.21 \pm 0.03\text{‰}$, $\Delta^{200}\text{Hg}$: $-0.06 \pm 0.00\text{‰}$, $n = 3$) (Fig. 4). This positive $\delta^{202}\text{Hg}$ first reflects a mixture of snow (0.74‰) and ocean emissions (-0.21‰), and both sources have negative $\Delta^{199}\text{Hg}$ (-0.53‰ to -0.25‰) values (Table 1) (Jiskra et al., 2019; Sherman et al., 2010). More important, Hg(0) dry deposition to tundra and snowpack plays a key role in positively shifting air $\delta^{202}\text{Hg}$ values (Douglas and Blum, 2019; Obrist et al., 2017), because these processes are accompanied by a large enrichment factor ($\epsilon_{MDF}^{202/198} = -4.22 \pm 1.01\text{‰}$) (Jiskra et al., 2019; Douglas and Blum, 2019).

The Antarctic ($>60^\circ\text{S}$) has a distinct Hg cycle from the Arctic with less vegetation and lower temperature, which may affect the Hg(0) sink, the redox chemistry, and eventually the Hg isotope fractionation (Yu et al., 2021; Li et al., 2020a). The modeled Hg composition in the Antarctic has positive $\delta^{202}\text{Hg}$ (0.54‰ – 0.90‰), negative $\Delta^{199}\text{Hg}$ (-0.28‰ to -0.21‰) and $\Delta^{200}\text{Hg}$ (-0.09‰ to -0.08‰). A recent study at the Antarctic Great Wall Station (GWS) (Yu et al., 2021) showed $\delta^{202}\text{Hg}$ range from 0.10‰ to 0.84‰ (mean: $0.57 \pm 0.20\text{‰}$), $\Delta^{199}\text{Hg}$ of -0.52‰ to -0.18‰ (mean: $-0.29 \pm 0.10\text{‰}$), and $\Delta^{200}\text{Hg}$ of -0.13‰ to -0.05‰ (mean: $-0.07 \pm 0.02\text{‰}$). In comparison, our simulation has both comparable MDF and MIF values at this site ($\delta^{202}\text{Hg}$: 0.31‰ , $\Delta^{199}\text{Hg}$: -0.26‰ , $\Delta^{200}\text{Hg}$: -0.09‰) (Fig. 4a, b, and c).

3.4. Zonal distribution

Our model also predicts the Hg isotope values in the free troposphere (Fig. 5). We find the modeled spatial distribution of the zonal mean isotope values largely reflects the spatial patterns of Hg emissions and its redox chemistry. For $\delta^{202}\text{Hg}$ and $\Delta^{200}\text{Hg}$, a latitudinal gradient is modeled near the ground surface (Fig. 5a and c) and the gradient decreases as altitude increases due to air mixing. However, we note the modeled $\Delta^{200}\text{Hg}$ has a narrow range and is close to the detection limit of isotope measurement. The $\delta^{202}\text{Hg}$ has a relatively lower zone in the upper tropic troposphere, where Hg(II) concentrations are high and Hg redox is the strongest (Horowitz et al., 2017). By contrast, both $\Delta^{199}\text{Hg}$ (Fig. 5b) and $\Delta^{201}\text{Hg}$ (Fig. 5d) have distinct patterns with higher values over the equatorial troposphere (15°S to 15°N) ($\Delta^{199}\text{Hg}$: $-0.24 \pm 0.02\text{‰}$, $\Delta^{201}\text{Hg}$: $-0.23 \pm 0.02\text{‰}$), which are related to the redox chemistry as discussed below. There is a general scarcity of isotope data in the free troposphere. Fu et al. (2016) measured the isotope composition of gaseous mercury in the free troposphere of the Pic du Midi (43.06°N , 2860 m), with the $\delta^{202}\text{Hg}$ of $-0.34 \pm 0.10\text{‰}$, $\Delta^{199}\text{Hg}$ of $-0.22 \pm 0.06\text{‰}$, $\Delta^{200}\text{Hg}$ of $-0.08 \pm 0.05\text{‰}$, and $\Delta^{201}\text{Hg}$ of $-0.20 \pm 0.05\text{‰}$. Our model agrees well with the observed MDF and odd-MIF, but not with the even-MIF. This is likely because the used even-MIF scheme

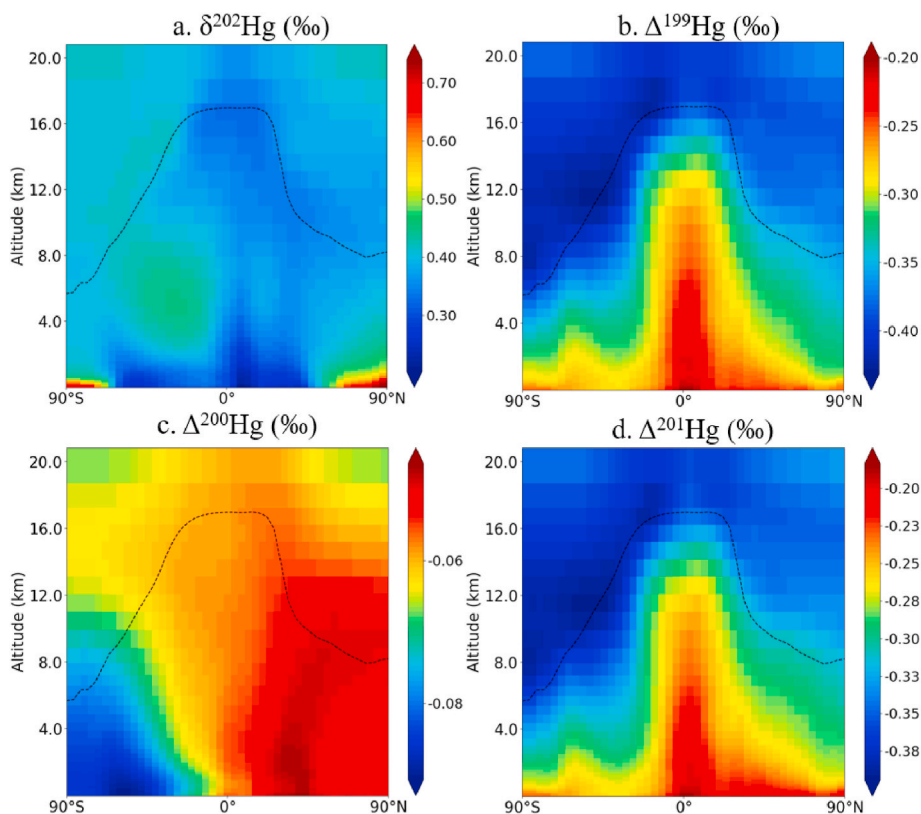


Fig. 5. The zonal mean of TGM isotope composition in the atmosphere.

in the model is not representative.

The $\Delta^{200}\text{Hg}$ pattern overall is a consequence of the source mixture due to the minuscule fractionation of even-MIF in the model (Fig. 1) (Sun et al., 2016a). Lower $\Delta^{200}\text{Hg}$ values in SH are affected by the ocean emission that is -0.11‰ in the model (Table 1), while the NH emissions have higher $\Delta^{200}\text{Hg}$ values due to lower ocean emissions (Fig. A1, Table 1). The $\delta^{202}\text{Hg}$ and odd-MIF patterns, however, reflect the competition between oxidation and reduction processes, and to a less extent, reflect the influence of gas-particle partitioning and wet removal

processes in the atmosphere. We find that the odd-MIF of TGM is anti-correlated with the Hg(II) mixing ratio (Fig. A2a), which is largely influenced by the distribution of Br and BrO (Fig. A2b and S2c). The Hg(0) oxidation process causes a positive $\delta^{202}\text{Hg}$ and odd-MIF in the remaining Hg(0), but the magnitude of this fractionation is much smaller than the Hg(II) reduction process, which causes a negative $\delta^{202}\text{Hg}$ and odd-MIF in Hg(0) (Fig. A3a) and positive odd-MIF in Hg(II)_g and Hg(II)_p (Fig. A3b) (Yuan et al., 2019; Zheng and Hintelmann, 2010, 2009). Besides, redox chemistry has comparable oxidation rates and

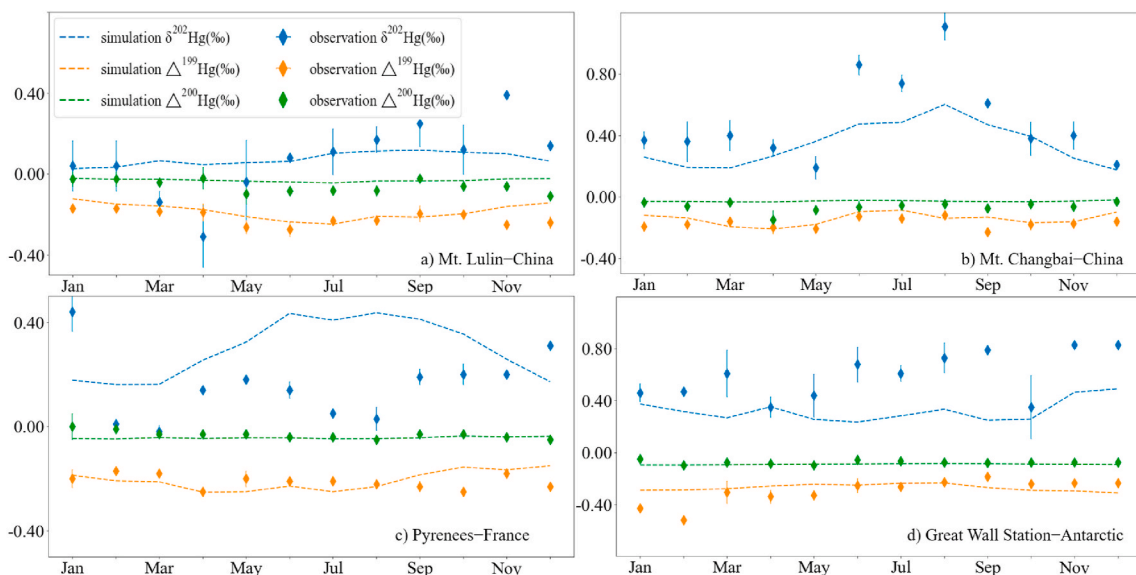


Fig. 6. Annual temporal variation in Hg isotope composition of TGM. Observations are cited from (a) Nguyen et al. (2021), (b) Fu et al. (2019), (c) Fu et al. (2016), and (d) Yu et al. (2021).

reduction rates in the upper atmosphere (Fig. A3c, A3d). Considering the mass conservation of total Hg [TGM + Hg(II)_p], the enriched ²⁰²Hg and odd-Hg in Hg(II)_p thus imply a depletion of ²⁰²Hg and odd-Hg in TGM (Fig. A3c). The wet removal of Hg(II) also reinforces the decrease of these Hg isotopes in TGM.

3.5. Seasonal variability

Fig. 6 shows the simulated seasonal variations of $\delta^{202}\text{Hg}$, $\Delta^{199}\text{Hg}$, and $\Delta^{200}\text{Hg}$ for TGM, compared against observations at two sites in China, one site in France, and one site in the Antarctic. The simulated $\delta^{202}\text{Hg}$ (−0.4‰–1.1‰) has much larger variability than $\Delta^{199}\text{Hg}$ (−0.4‰ to −0.1‰) and $\Delta^{200}\text{Hg}$ (−0.1‰–0.0‰) at all these four sites. The modeled $\delta^{202}\text{Hg}$ at Mt. Lulin (Fig. 6a) and Mt. Changbai (Fig. 6b) are both consistent with observations (Nguyen et al., 2021; Fu et al., 2019), with the maximum values from May to October. The observed variabilities of $\delta^{202}\text{Hg}$ in Mt. Lulin and Mt. Changbai are attributed to vegetation uptake, as the measured $\delta^{202}\text{Hg}$ is highly correlated with normalized difference vegetation index (NDVI) (Nguyen et al., 2021; Fu et al., 2019), which indicates intense vegetation activities during boreal summer. In our model, we also find a significant correlation between the seasonal $\delta^{202}\text{Hg}$ and LAI at these two sites (Fig. A4), which confirms that our model can capture the vegetation uptake effect and the global vegetation may have a significant impact on the atmospheric $\delta^{202}\text{Hg}$. The simulated $\delta^{202}\text{Hg}$ is a little higher at the Pyrenees (Fig. 6c) and lower at the GWS (Fig. 6d). The observed $\delta^{202}\text{Hg}$ at the Pyrenees resulted from the mixing of European anthropogenic emissions (lower) and the North Atlantic Ocean (higher) (Fu et al., 2016). Whereas, the observed $\delta^{202}\text{Hg}$ at the GWS is dominated by the inland katabatic wind in the austral winter and by sea-ice dynamics in the austral summer (Yu et al., 2021). We speculated that the disparities in our model may be caused by two factors. The first factor is the coarse model resolution that biases high toward the contribution of ocean-sourced Hg. The second factor is the uncertainties of the isotope composition of ocean emission and the fractionation in redox chemistry.

The simulated $\Delta^{199}\text{Hg}$ are close to the observations at four sites, both in the magnitude and seasonal trends. The variabilities of $\Delta^{199}\text{Hg}$ in Mt. Lulin and GWS are relatively small, resulting from the mixture of

continental and marine air masses (Yu et al., 2021; Nguyen et al., 2021). $\Delta^{199}\text{Hg}$ in Mt. Changbai is related to the intense vegetation photosynthetic activity in the sunniest season (Fu et al., 2019). Overall, the agreement with these observations indicates that our model can simulate these processes and their seasonal variability reasonably well.

3.6. Budgets of isotopes

Fig. 7 shows the modeled Hg budgets in the global atmosphere with their isotope signatures. The modeled global atmospheric Hg mass is 3700 Mg, including ~3500 Mg of Hg(0) and ~200 Mg of Hg(II). The total oxidation rate from Hg(0) to Hg(II) is ~13000 Mg with a total reduction rate of ~7500 Mg. The lifetime of global TGM against deposition is 5.0 months, Hg(0) against oxidation is 3.2 months, and Hg(II) against reduction is 11 days. These results are consistent with previous studies (Horowitz et al., 2017). We also calculate the lifetime of each isotope relative to ¹⁹⁸Hg (Fig. A5). We find that ¹⁹⁹Hg(II) and ²⁰¹Hg(II) have a relatively longer lifetime against reduction, which leads to the enrichment of these two isotopes in Hg(II). This also shortens the TGM lifetime of these two isotopes against deposition due to the faster removal of Hg(II) than Hg(0).

The global Hg(0) pool has $\delta^{202}\text{Hg}$ of 0.36‰, $\Delta^{199}\text{Hg}$ of −0.30‰, and $\Delta^{200}\text{Hg}$ of −0.06‰, while the Hg(II) pool shows lower $\delta^{202}\text{Hg}$ of 0.05‰, positive $\Delta^{199}\text{Hg}$ of 0.37‰, and identical $\Delta^{200}\text{Hg}$ of −0.06‰. The modeled Hg(0) are isotopically comparable to global observations ($\delta^{202}\text{Hg}$: $-0.08 \pm 0.51\%$; $\Delta^{199}\text{Hg}$: $-0.12 \pm 0.09\%$; $\Delta^{200}\text{Hg}$: $-0.03 \pm 0.03\%$) in TGM [dominated by Hg(0)], and the MIF also consistent with the simulated results of Sun et al. (2019) using a box model ($\Delta^{199}\text{Hg}$: -0.11% ; $\Delta^{200}\text{Hg}$: -0.04%). We find that the atmospheric $\delta^{202}\text{Hg}$ (0) is much higher than the total emissions (−0.53‰), which is mainly caused by the Hg(0) deposition and oxidation processes, leading to strong enrichment of heavier isotopes in Hg(0). The $\delta^{202}\text{Hg}$ of Hg(II) should be transformed from the MDF due to oxidation (−0.41‰), but a strong MDF associated with photo-reduction (−0.69‰) has shifted the Hg(II) pool to a heavier $\delta^{202}\text{Hg}$ of 0.05‰. For $\Delta^{199}\text{Hg}$ (0), the magnitude associated with oxidation (−0.55‰) is much smaller than reduction (−1.04‰). We thus suggest that atmospheric Hg(II) reduction dominates $\Delta^{199}\text{Hg}$ in both Hg(0) and Hg(II) pool, which shifts the Hg(0) pool

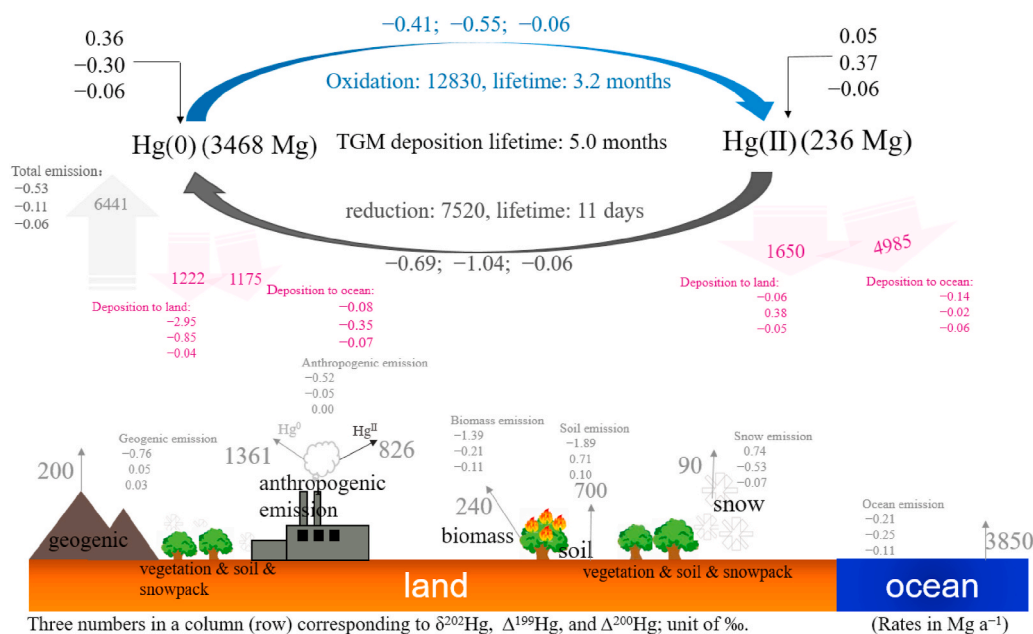


Fig. 7. Global Atmospheric Hg budgets and Hg isotope compositions. The arrows represent transformation fluxes of Hg and their isotope compositions. The MDF, odd-MIF, and even-MIF are represented by $\delta^{202}\text{Hg}$, $\Delta^{199}\text{Hg}$, and $\Delta^{200}\text{Hg}$ respectively. The grey-colored arrows and numbers represent emissions to the atmosphere, and the purple ones for atmospheric Hg deposition to land and ocean.

to a more negative value (-0.30‰) than the source emission (-0.11‰) and shifts the Hg(II) pool to a more positive $\Delta^{199}\text{Hg}$ (0.37‰). Furthermore, Hg(II) deposition on land has higher $\delta^{202}\text{Hg}$ (-0.06‰) and $\Delta^{199}\text{Hg}$ (0.38‰) than to the ocean ($\delta^{202}\text{Hg}$: -0.14‰ , $\Delta^{199}\text{Hg}$: -0.02‰) due to higher photo-reduction rates of atmospheric Hg(II) (Fig. A6a) and higher oxidation rates (Fig. A6b) on land. The $\Delta^{200}\text{Hg}$ in Hg (II) pool (-0.06‰) does not reproduce the observed $\Delta^{200}\text{Hg}$ ($\sim 0.17\text{‰}$) in rainfall (Sun et al., 2019), because the model only uses a small fractionation factor of 0.06‰ during Cl-oxidation, which merits further examination in our future studies.

3.7. Relationships among isotope values

The isotope compositions of simulated surface TGM (each model grid as an individual dot) are plotted in Fig. 8a, as compared to the primary emissions and re-emissions (circle and triangle), and observations (square). Overall, the TGM data for simulations and the observations occupy similar ranges in the $\Delta^{199}\text{Hg}$ - $\delta^{202}\text{Hg}$ plot, and our model results fall within the uncertainty range of observations on a global scale. Simulated data in the NH are more dispersed, caused by the diverse sources, whereas the data for SH are relatively concentrated, mainly impacted by ocean emissions.

The regression slope of $\Delta^{199}\text{Hg}$ - $\Delta^{201}\text{Hg}$ plots for TGM provides further information for atmospheric Hg redox processes (Fig. 8b) (Yu et al., 2021; Kurz et al., 2021; Fu et al., 2021a; Yuan et al., 2020; Yu

et al., 2020). The fitted slope of the simulated data is 1.02, consistent with the global atmospheric Hg observations (1.01), but lower than 1.19 that is the slope for the sum of primary and re-emitted Hg. The Hg(0) oxidation and Hg(II) photo-reduction processes compete in driving this slope. Hg(0) oxidation by Br and Cl have a slope of 1.64 and 1.89, respectively (Sun et al., 2016a), which drives the slope to a relatively high value. In contrast, photo-reduction shifts the slope to a lower value (1.00) (Blum et al., 2014). The fact that the modeled slope is closer to the photo-reduction slope suggests that the photo-reduction of Hg(II) is the main control of the odd-MIF in global TGM, consistent with previous studies in surface waters and cloud droplets (Bergquist, 2018).

3.8. Sensitivity to fractionation factors

Our model can be used as a diagnostic tool to test the effect of individual fractionation processes on Hg isotope compositions in the atmosphere. The results are also an indicator of the model uncertainty. As a demonstration, we evaluate the impacts of isotope fractionation for Hg(0) dry deposition to land, Hg(0) oxidation, and Hg(II) photo-reduction, which are important processes for atmospheric Hg fractionation but their reported enrichment factors (ϵ) have large uncertainties. The MDF enrichment factors for vegetation uptake have been reported to have a large interval, from -1‰ to -4‰ (Jiskra et al., 2019; Obrist et al., 2017; Enrico et al., 2016), while that for Hg(0) oxidation ranges from -0.85‰ to 0.74‰ . The isotope enrichment factors of photo-reduction of atmospheric aqueous-phase Hg(II) have not been directly reported yet, but they could range from -1.80‰ to -0.55‰ for $\epsilon_{MDF}^{202/198}$, and from -6.61‰ to 1.02‰ for $\epsilon_{MIF}^{199/198}$ if they are extrapolated from those of experimental aquatic dissolved Hg(II) (Zheng and Hintelmann, 2010; Bergquist and Blum, 2007; Zheng and Hintelmann, 2009; Yang and Sturgeon, 2009; Rose et al., 2015; Bergquist and Blum, 2009). In sensitivity simulations, we perturb these enrichment factors alternatively by a factor of two relative to our default values in the models (other parameters are held constant) and then evaluate their impact on Hg isotope distribution.

Fig. 9 shows the shifted values after the factor of two increases of enrichment factors (the results with a factor of two decreases are shown in Fig. A7). In general, we find that increasing $\epsilon_{MDF}^{202/198}$ values of Br oxidation and Hg(0) dry deposition (to land) enriches more heavy isotopes in Hg(0), shifting the $\delta^{202}\text{Hg}$ in TGM toward positive values. In contrast, increasing the fractionation factors of Hg(II) reduction would shift the $\delta^{202}\text{Hg}$ in TGM toward negative values. The shifted values by dry deposition and Br oxidation are all substantial, indicating that the currently observed isotope compositions of TGM can well constrain the $\delta^{202}\text{Hg}$ fractionation magnitude of these processes. This alternatively supports the fitted enrichment factor ($\epsilon_{MDF}^{202/198} = -0.85\text{‰}$) of Sun et al. (2019) is more representative of our model that treats the net redox chemistry effect. Increasing $\epsilon_{MDF}^{202/198}$ for Hg(0) dry deposition to land also induces an increase of $\delta^{202}\text{Hg}$, with a higher increase over land ($+0.79 \pm 0.21\text{‰}$) than over the ocean ($+0.62 \pm 0.22\text{‰}$). The underestimation of $\delta^{202}\text{Hg}$ by our model at some forest sites thus may result from an underestimate of the enrichment factor of vegetation uptake.

The shift of $\Delta^{199}\text{Hg}$ by Br oxidation and Hg(0) dry deposition is relatively small (Fig. 9). However, the Hg(II) photo-reduction process results in the largest shift on $\Delta^{199}\text{Hg}$ (global mean of $-0.37 \pm 0.06\text{‰}$), indicating $\Delta^{199}\text{Hg}$ in TGM is most sensitive to this process. The enrichment factor of $\epsilon_{MIF}^{199/198}$ for Hg(II) reduction is set as -2.17‰ in this study. The agreement between the simulated and observed $\Delta^{199}\text{Hg}$ thus suggests that this is a reasonable assumption for this factor.

Additionally, we also conduct the same sensitivity simulations for the isotope signature of ocean re-emission. Large variations of $\delta^{202}\text{Hg}$ for marine-sourced Hg(0) are suggested in previous studies (-3.88‰ – 0.77‰) (Fu et al., 2016; Jiskra et al., 2015; Rolison et al., 2013; Fu et al.,

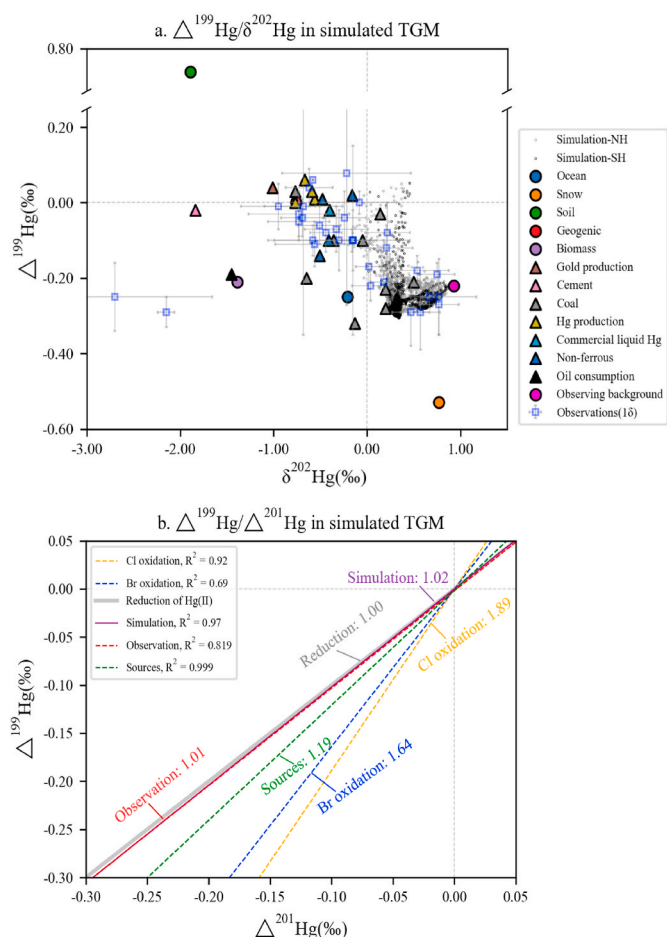


Fig. 8. Isotopic compositions of global surface TGM and in the model. (a) $\Delta^{199}\text{Hg}$ vs. $\delta^{202}\text{Hg}$, with the dots representing simulation in NH and SH, the circles representing natural and re-emission sources, the triangles representing anthropogenic sources, and the squares representing the observations. (b) The slopes of $\Delta^{199}\text{Hg}$ vs. $\Delta^{201}\text{Hg}$. The Br/Cl oxidations are cited from Sun et al. (2016a), and photo-reduction of Hg(II) is cited from Blum et al. (2014).

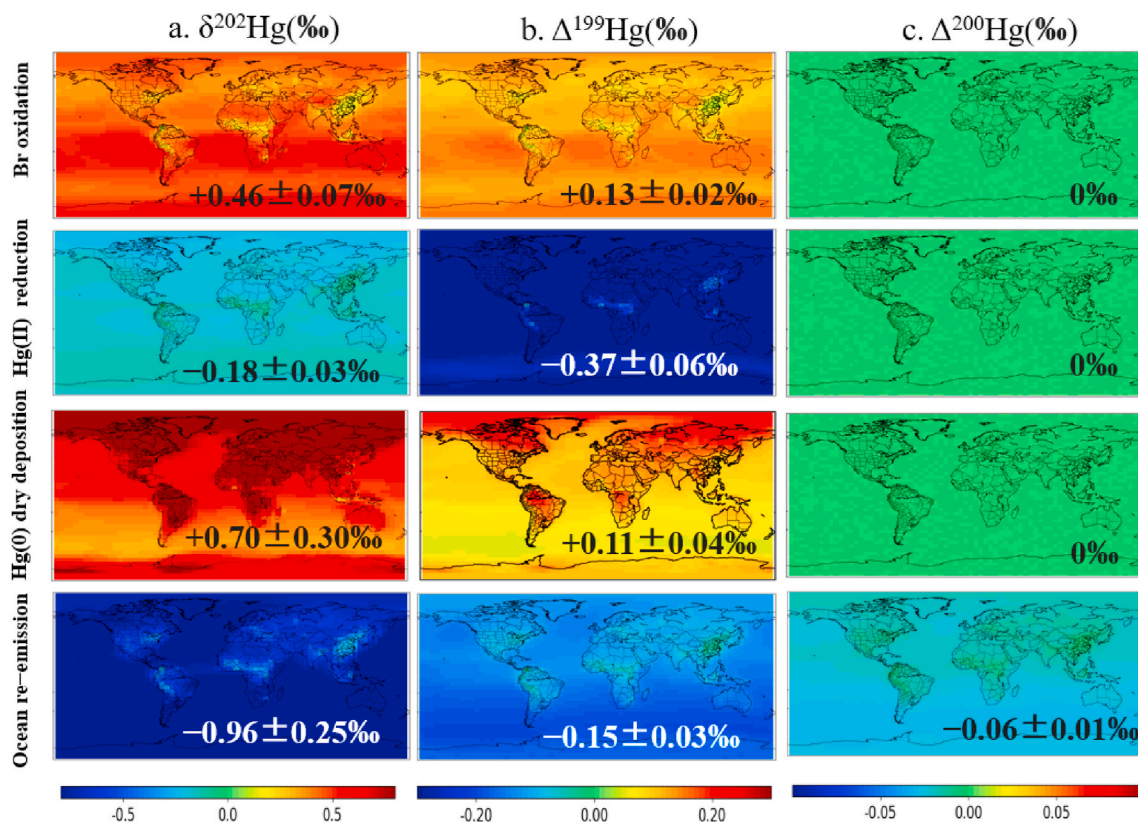


Fig. 9. Model sensitivity to the factor of two increases of enrichment factors (ϵ). Column (a), (b), and (c) is for MDF, odd-MIF, and even-MIF, respectively. For each column, the panels show the global differences between original and increasing the enrichment factors by a factor of two for the four processes (from top to bottom): Br oxidation, Hg(II) reduction, Hg(0) dry deposition, and ocean re-emission.

2018), and we assume it to be -0.21‰ in the model. The model reveals a significant impact of ocean re-emission on $\delta^{202}\text{Hg}$ of global TGM. The $\delta^{202}\text{Hg}$ is shifted by $-0.96 \pm 0.25\text{‰}$ (i.e., a factor of two increase) if the re-emission is set to -0.42‰ (Fig. 9), and is shifted by $+0.47 \pm 0.12\text{‰}$ (i.e., a factor of two decrease) if the re-emission is set to -0.11‰ (Fig. A7). We therefore call for more studies to constrain the Hg isotope composition of ocean emission, which is critical for our understanding of its global impact on the $\delta^{202}\text{Hg}$ of TGM. The $\Delta^{199}\text{Hg}$ in TGM is influenced to a limited extent ($-0.15 \pm 0.03\text{‰}$) by ocean re-emissions when compared with Hg(II) reduction ($-0.37 \pm 0.06\text{‰}$). The ocean re-emission can slightly shift the $\Delta^{200}\text{Hg}$ in TGM ($-0.06 \pm 0.01\text{‰}$) because a $\Delta^{200}\text{Hg}$ of -0.11‰ (Table 1) is used for this source. While a recent study (Jiskra et al., 2021) has reported a slightly positive (0.02‰) ocean $\Delta^{200}\text{Hg}$, it merits further evaluation.

4. Conclusions

We develop a 3-D atmospheric Hg isotope model based on the GEOS-Chem model platform. By integrating with source emissions and process-based fractionations, the model simulates the Hg isotope compositions in the global atmosphere, which generally agrees with available observations. The global distribution pattern of modeled Hg isotope composition in TGM is largely impacted by source emissions and redox chemistry. In general, TGM over the ocean is characterized by lower $\Delta^{199}\text{Hg}$ than that over land. Anthropogenic emission and soil re-emission mainly impact the populated regions, where the $\delta^{202}\text{Hg}$ and $\Delta^{199}\text{Hg}$ tend to have negative and near-zero values, respectively. TGM in polar regions is isotopically impacted by Hg(0) dry deposition and snowpack re-emission. Atmospheric processes can reshape the atmospheric Hg isotope composition. The $\delta^{202}\text{Hg}$ in global TGM is mostly impacted by Hg(0) uptake by vegetation, and the $\Delta^{199}\text{Hg}$ is mostly impacted by photo-reduction of atmospheric Hg(II).

Our ability to simulate the isotope compositions in global TGM is limited by existing scientific knowledge and data. There is still significant uncertainty in the current mechanistic model, such as the atmospheric Hg redox chemistry, Hg(0) uptake by vegetation, and land/ocean re-emissions (e.g., Obrist et al., 2021; Jiskra et al., 2021). The missing isotope fractionation information of chemical and physical processes adds another layer of uncertainty. We therefore call for more studies on these issues. Our model can be treated as a demonstration of the potential of the 3D model in interpolating atmospheric isotope measurements. It is a test-bed that can bring together the observations and fractionation mechanisms and test whether the observations can be reproduced by the known theories.

Credit author statement

Zhengcheng Song: Methodology, Validation, Formal analysis, Data Curation, Writing - Original Draft, Writing - Review & Editing, Visualization. Ruoyu Sun: Methodology, Resources, Writing - Review & Editing. Yanxu Zhang: Methodology, Conceptualization, Writing - Review & Editing, Supervision, Project administration, Funding acquisition.

Declaration of competing interest

The authors declare that they have no known competing financial interests or personal relationships that could have appeared to influence the work reported in this paper.

Acknowledgments

This study was supported by the National Key Research & Development Program of China (grant no. 2019YFA0606803), the Fundamental Research Funds for the Central Universities (grant no. 020714380188,

020714380168), and Frontiers Science Center for Critical Earth Material Cycling.

Appendix A. Supplementary data

Supplementary data to this article can be found online at <https://doi.org/10.1016/j.envpol.2022.119588>.

References

- Amos, H.M., Jacob, D.J., Holmes, C.D., Fisher, J.A., Wang, Q., Yantosca, R.M., Corbitt, E. S., Galarrneau, E., Rutter, A.P., Gustin, M.S., Steffen, A., Schauer, J.J., Graydon, J.A., Louis, V.L.S., Talbot, R.W., Edgerton, E.S., Zhang, Y., Sunderland, E.M., 2012. Gas-particle partitioning of atmospheric Hg(II) and its effect on global mercury deposition. *Atmos. Chem. Phys.* 12, 591–603. <https://doi.org/10.5194/acp-12-591-2012>.
- Amos, H.M., Jacob, D.J., Streets, D.G., Sunderland, E.M., 2013. Legacy impacts of all-time anthropogenic emissions on the global mercury cycle. *Global Biogeochem. Cycles* 27, 410–421. <https://doi.org/10.1002/gbc.20040>.
- Ariya, P.A., Dastoor, A.P., Amyot, M., Schroeder, W.H., Barrie, L., Anlauf, K., Raofie, F., Ryzhkov, A., Davignon, D., Lalonde, J., Steffen, A., 2004. The Arctic: a sink for mercury. *Tellus Ser. B Chem. Phys. Meteorol.* 56, 397–403. <https://doi.org/10.1111/j.1600-0889.2004.00118.x>.
- Bergquist, B.A., Blum, J.D., 2007. Mass-dependent and -independent fractionation of Hg isotopes by photoreduction in aquatic systems. *Science* 318, 417–420. <https://doi.org/10.1126/science>.
- Bergquist, B.A., Blum, J.D., 2009. The odds and evens of mercury isotopes: applications of mass-dependent and mass-independent isotope fractionation. *Elements* 5, 353–357. <https://doi.org/10.2113/gselements.5.6.353>.
- Bergquist, B.A., 2018. Mercury isotopes. In: *Encyclopedia of Engineering Geology, Encyclopedia of Earth Sciences Series, vols. 1–7*.
- Bieser, J., Angot, H., Slemr, F., Martin, L., 2020. Atmospheric mercury in the southern Hemisphere - Part 2: source apportionment analysis at Cape point station, South Africa. *Atmos. Chem. Phys.* 20, 10427–10439. <https://doi.org/10.5194/acp-20-10427-2020>.
- Blum, J.D., Bergquist, B.A., 2007. Reporting of variations in the natural isotopic composition of mercury. *Anal. Bioanal. Chem.* 388, 353–359. <https://doi.org/10.1007/s00216-007-1236-9>.
- Blum, J.D., 2012. Applications of stable mercury isotopes to biogeochemistry. In: *Handbook of Environmental Isotope Geochemistry*, pp. 229–245.
- Blum, J.D., Sherman, L.S., Johnson, M.W., 2014. Mercury isotopes in earth and environmental sciences. *Annu. Rev. Earth Planet Sci.* 42, 249–269. <https://doi.org/10.1146/annurev-earth-050212-124107>.
- Blum, J.D., Johnson, M.W., 2017. Recent developments in mercury stable isotope analysis. *Rev. Mineral. Geochem.* 82, 733–757. <https://doi.org/10.2138/rmg.2017.82.17>.
- Chen, J.B., Hintelmann, H., Feng, X.B., Dimock, B., 2012. Unusual fractionation of both odd and even mercury isotopes in precipitation from Peterborough, ON, Canada. *Geochim. Cosmochim. Acta* 90, 33–46. <https://doi.org/10.1016/j.gca.2012.05.005>.
- Demers, J.D., Blum, J.D., Zak, D.R., 2013. Mercury isotopes in a forested ecosystem: implications for air-surface exchange dynamics and the global mercury cycle. *Global Biogeochem. Cycles* 27, 222–238. <https://doi.org/10.1002/gbc.20021>.
- Demers, J.D., Sherman, L.S., Blum, J.D., Marsik, F.J., Dvonch, J.T., 2015. Coupling Atmospheric Mercury Isotope Ratios and Meteorology to Identify Sources of Mercury Impacting a Coastal Urban-Industrial Region Near Pensacola, vol. 29. *Global Biogeochemical Cycles, Florida, USA*, pp. 1689–1705. <https://doi.org/10.1002/2015gb005146>.
- Douglas, T.A., Blum, J.D., 2019. Mercury isotopes reveal atmospheric gaseous mercury deposition directly to the Arctic coastal snowpack. *Environ. Sci. Technol. Lett.* 6, 235–242. <https://doi.org/10.1021/acs.estlett.9b00131>.
- Driscoll, C.T., Mason, R.P., Chan, H.M., Jacob, D.J., Pirrone, N., 2013. Mercury as a global pollutant: sources, pathways, and effects. *Environ. Sci. Technol.* 47, 4967–4983. <https://doi.org/10.1021/es305071v>.
- Enrico, M., Le Roux, G., Maruszczak, N., Heimbürger, L.E., Claustres, A., Fu, X.W., Sun, R. Y., Sonke, J.E., 2016. Atmospheric mercury transfer to peat bogs dominated by gaseous elemental mercury dry deposition. *Environ. Sci. Technol.* 50, 2405–2412. <https://doi.org/10.1021/acs.est.5b06058>.
- Fu, X., Maruszczak, N., Wang, X., Gheusi, F., Sonke, J.E., 2016. Isotopic composition of gaseous elemental mercury in the free troposphere of the Pic du Midi observatory, France. *Environ. Sci. Technol.* 50, 5641–5650. <https://doi.org/10.1021/acs.est.6b00033>.
- Fu, X., Yang, X., Tan, Q., Ming, L., Lin, T., Lin, C.-J., Li, X., Feng, X., 2018. Isotopic composition of gaseous elemental mercury in the marine boundary layer of east China sea. *J. Geophys. Res. Atmos.* 123, 7656–7669. <https://doi.org/10.1029/2018jd028671>.
- Fu, X., Zhang, H., Liu, C., Zhang, H., Lin, C.J., Feng, X., 2019. Significant seasonal variations in isotopic composition of atmospheric total gaseous mercury at forest sites in China caused by vegetation and mercury sources. *Environ. Sci. Technol.* 53, 13748–13756. <https://doi.org/10.1021/acs.est.9b05016>.
- Fu, X., Jiskra, M., Yang, X., Maruszczak, N., Enrico, M., Chmeleff, J., Heimbürger-Boavida, L.E., Gheusi, F., Sonke, J.E., 2021a. Mass-independent fractionation of even and odd mercury isotopes during atmospheric mercury redox reactions. *Environ. Sci. Technol.* 55, 10164–10174. <https://doi.org/10.1021/acs.est.1c02568>.
- Fu, X., Liu, C., Zhang, H., Xu, Y., Zhang, H., Li, J., Lyu, X., Zhang, G., Guo, H., Wang, X., Zhang, L., Feng, X., 2021b. Isotopic compositions of atmospheric total gaseous mercury in 10 Chinese cities and implications for land surface emissions. *Atmos. Chem. Phys.* 21, 6721–6734. <https://doi.org/10.5194/acp-21-6721-2021>.
- Gencarelli, C.N., Bieser, J., Carbone, F., De Simone, F., Hedgecock, I.M., Matthias, V., Travníkov, O., Yang, X., Pirrone, N., 2017. Sensitivity model study of regional mercury dispersion in the atmosphere. *Atmos. Chem. Phys.* 17, 627–643. <https://doi.org/10.5194/acp-17-627-2017>.
- Gratz, L.E., Keeler, G.J., Blum, J.D., Sherman, L.S., 2010. Isotopic composition and fractionation of mercury in Great Lakes precipitation and ambient air. *Environ. Sci. Technol.* 44, 7764–7770. <https://doi.org/10.1021/es100383w>.
- Hintelmann, H., Zheng, W., 2011. Tracking geochemical transformations and transport of mercury through isotope fractionation. In: Liu, G., Cai, Y., O'Driscoll, N. (Eds.), *Environmental Chemistry and Toxicology of Mercury*. John Wiley & Sons, Hoboken, pp. 293–328.
- Holmes, C.D., Jacob, D.J., Mason, R.P., Jaffe, D.A., 2009. Sources and deposition of reactive gaseous mercury in the marine atmosphere. *Atmos. Environ.* 43, 2278–2285. <https://doi.org/10.1016/j.atmosenv.2009.01.051>.
- Holmes, C.D., Jacob, D.J., Corbitt, E.S., Mao, J., Yang, X., Talbot, R., Slemr, F., 2010. Global atmospheric model for mercury including oxidation by bromine atoms. *Atmos. Chem. Phys.* 10, 12037–12057. <https://doi.org/10.5194/acp-10-12037-2010>.
- Horowitz, H.M., Jacob, D.J., Zhang, Y., Dibble, T.S., Slemr, F., Amos, H.M., Schmidt, J. A., Corbitt, E.S., Marais, E.A., Sunderland, E.M., 2017. A new mechanism for atmospheric mercury redox chemistry: implications for the global mercury budget. *Atmos. Chem. Phys.* 17, 6353–6371. <https://doi.org/10.5194/acp-17-6353-2017>.
- Huang, S., Zhang, Y., 2021. Interannual variability of air-sea exchange of mercury in the global ocean: the "seesaw effect" in the equatorial Pacific and contributions to the atmosphere. *Environ. Sci. Technol.* 55, 7145–7156. <https://doi.org/10.1021/acs.est.1c00691>.
- Jacob, D.J., Wofsy, S.C., 1990. Budgets of reactive nitrogen, hydrocarbons, and ozone over the Amazon-Forest during the wet season. *Grammarly* 95, 16737–16754. <https://doi.org/10.1029/JD095iD10p16737>.
- Jacob, D.J., Fan, S.M., Wofsy, S.C., Spiro, P.A., Bakwin, P.S., Ritter, J.A., Browell, E.V., Gregory, G.L., Fitzjarrald, D.R., Moore, K.E., 1992. Deposition of ozone to tundra. *J. Geophys. Res. Atmos.* 97, 16473–16479. <https://doi.org/10.1029/91jd02696>.
- Jiskra, M., Wiederhold, J.G., Skyllberg, U., Kronberg, R.M., Hajdas, I., Kretzschmar, R., 2015. Mercury deposition and re-emission pathways in boreal forest soils investigated with Hg isotope signatures. *Environ. Sci. Technol.* 49, 7188–7196. <https://doi.org/10.1021/acs.est.5b00742>.
- Jiskra, M., Sonke, J.E., Obrist, D., Bieser, J., Ebinghaus, R., Myhre, C.L., Pfaffhuber, K.A., Wangberg, I., Kyllonen, K., Worthy, D., Martin, L.G., Labuschagne, C., Mkololo, T., Ramonet, M., Magand, O., Dommargue, A., 2018. A vegetation control on seasonal variations in global atmospheric mercury concentrations. *Nat. Geosci.* 11, 244. <https://doi.org/10.1038/s41561-018-0078-8>.
- Jiskra, M., Sonke, J.E., Agnan, Y., Helmig, D., Obrist, D., 2019. Insights from mercury stable isotopes on terrestrial-atmosphere exchange of Hg(0) in the Arctic tundra. *Biogeosciences* 16, 4051–4064. <https://doi.org/10.5194/bg-16-4051-2019>.
- Jiskra, M., Heimbürger-Boavida, L.-E., Desgranges, M.-M., Petrova, M.V., Dufour, A., Ferreira-Araújo, B., Masbou, J., Chmeleff, J., Thyssen, M., Point, D., Sonke, J.E., 2021. Mercury stable isotopes constrain atmospheric sources to the ocean. *Nature* 597, 678–682. <https://doi.org/10.1038/s41586-021-03859-8>.
- Koster van Groos, P.G., Esser, B.K., Williams, R.W., Hunt, J.R., 2014. Isotope effect of mercury diffusion in air. *Environ. Sci. Technol.* 48, 227–233. <https://doi.org/10.1021/es4033666>.
- Kurz, A.Y., Blum, J.D., Gratz, L.E., Jaffe, D.A., 2020. Contrasting controls on the diel isotopic variation of Hg(0) at two high elevation sites in the Western United States. *Environ. Sci. Technol.* 54, 10502–10513. <https://doi.org/10.1021/acs.est.0c01918>.
- Kurz, A.Y., Blum, J.D., Johnson, M.W., Nadelhoffer, K., Zak, D.R., 2021. Isotopic composition of mercury deposited via snow into mid-latitude ecosystems. *Sci. Total Environ.* vol. 784 <https://doi.org/10.1016/j.scitotenv.2021.147252>.
- Kwon, S.Y., Blum, J.D., Yin, R., Tsui, M.T.-K., Yang, Y.H., Choi, J.W., 2020. Mercury stable isotopes for monitoring the effectiveness of the Minamata Convention on Mercury. *Earth Sci. Rev.* 203 <https://doi.org/10.1016/j.earscirev.2020.103111>.
- Li, C.J., Chen, J.B., Angot, H., Zheng, W., Shi, G.T., Ding, M.H., Du, Z.H., Zhang, Q.G., Ma, X.Y., Kang, S.C., Xiao, C.D., Ren, J.W., Qin, D.H., 2020a. Seasonal variation of mercury and its isotopes in atmospheric particles at the coastal Zhongshan Station, eastern Antarctica. *Environ. Sci. Technol.* 54, 11344–11355. <https://doi.org/10.1021/acs.est.0c04462>.
- Li, C.X., Sonke, J.E., Le Roux, G., Piotrowska, N., Van der Putten, N., Roberts, S.J., Daley, T., Rice, E., Gehrels, R., Enrico, M., Mauquoy, D., Roland, T.P., De Vleeschouwer, F., 2020b. Unequal anthropogenic enrichment of mercury in earth's northern and southern hemispheres. *ACS Earth Space Chem* 4, 2073–2081. <https://doi.org/10.1021/acsearthspacechem.0c00220>.
- Li, X., Chen, J., Tang, L., Wu, T., Fu, C., Li, Z., Sun, G., Zhao, H., Zhang, L., Li, Q., Feng, X., 2021. Mercury isotope signatures of a pre-calciner cement plant in Southwest China. *J. Hazard Mater.* 401 <https://doi.org/10.1016/j.jhazmat.2020.123384>.
- Lin, J.T., McElroy, M.B., 2010. Impacts of boundary layer mixing on pollutant vertical profiles in the lower troposphere: implications to satellite remote sensing. *Atmos. Environ.* 44, 1726–1739. <https://doi.org/10.1016/j.atmosenv.2010.02.009>.
- Muntean, M., Janssens-Maenhout, G., Song, S., Giang, A., Selin, N.E., Zhong, H., Zhao, Y., Olivier, J.G.J., Guizzardi, D., Crippa, M., Schaaf, E., Dentener, F., 2018. Evaluating EDGARv4.4tox2 speciated mercury emissions ex-post scenarios and their impacts on modelled global and regional wet deposition patterns. *Atmos. Environ.* 184, 56–68. <https://doi.org/10.1016/j.atmosenv.2018.04.017>.

- Nguyen, L.S.P., Sheu, G.-R., Fu, X., Feng, X., Lin, N.-H., 2021. Isotopic composition of total gaseous mercury at a high-altitude tropical forest site influenced by air masses from the East Asia continent and the Pacific Ocean. *Atmos. Environ.* 246 <https://doi.org/10.1016/j.atmosenv.2020.118110>.
- Obrist, D., Agnan, Y., Jiskra, M., Olson, C.L., Colegrove, D.P., Hueber, J., Moore, C.W., Sonke, J.E., Helmig, D., 2017. Tundra uptake of atmospheric elemental mercury drives Arctic mercury pollution. *Nature* 547, 201. <https://doi.org/10.1038/nature22997>.
- Obrist, D., Roy, E.M., Harrison, J.L., Kwong, C.F., Munger, J.W., Moosmuller, H., Romero, C.D., Sun, S., Zhou, J., Commane, R., 2021. Previously unaccounted atmospheric mercury deposition in a midlatitude deciduous forest. *Proc. Natl. Acad. Sci. U. S. A* 118. <https://doi.org/10.1073/pnas.2105477118>.
- Pacyna, J.M., Travníkov, O., De Simone, F., Hedgecock, I.M., Sundseth, K., Pacyna, E.G., Steenhuisen, F., Pirrone, N., Munthe, J., Kindbom, K., 2016. Current and future levels of mercury atmospheric pollution on a global scale. *Atmos. Chem. Phys.* 16, 12495–12511. <https://doi.org/10.5194/acp-16-12495-2016>.
- Rolison, J.M., Landing, W.M., Luke, W., Cohen, M., Salters, V.J.M., 2013. Isotopic composition of species-specific atmospheric Hg in a coastal environment. *Chem. Geol.* 336, 37–49. <https://doi.org/10.1016/j.chemgeo.2012.10.007>.
- Rose, C.H., Ghosh, S., Blum, J.D., Bergquist, B.A., 2015. Effects of ultraviolet radiation on mercury isotope fractionation during photo-reduction for inorganic and organic mercury species. *Chem. Geol.* 405, 102–111. <https://doi.org/10.1016/j.chemgeo.2015.02.025>.
- Saiz-Lopez, A., Sitkiewicz, S.P., Roca-Sanjuan, D., Oliva-Enrich, J.M., Davalos, J.Z., Romero, C.D., Jiskra, M., Xu, Y., Wang, F., Thackray, C.P., Sunderland, E.M., Jacob, D.J., Travníkov, O., Cuevas, C.A., Acuna, A.U., Rivero, D., Plane, J.M.C., Kinnison, D.E., Sonke, J.E., 2018. Photoreduction of gaseous oxidized mercury changes global atmospheric mercury speciation, transport and deposition. *Nat. Commun.* 9, 4796. <https://doi.org/10.1038/s41467-018-07075-3>.
- Saiz-Lopez, A., Travníkov, O., Sonke, J.E., Thackray, C.P., Jacob, D.J., Carmona-García, J., Frances-Monerris, A., Roca-Sanjuan, D., Acuna, A.U., Davalos, J.Z., Cuevas, C.A., Jiskra, M., Wang, F., Bieser, J., Plane, J.M.C., Francisco, J.S., 2020. Photochemistry of oxidized Hg(I) and Hg(II) species suggests missing mercury oxidation in the troposphere. *Proc. Natl. Acad. Sci. U. S. A* 117, 30949–30956. <https://doi.org/10.1073/pnas.1922486117>.
- Schauble, E.A., 2007. Role of nuclear volume in driving equilibrium stable isotope fractionation of mercury, thallium, and other very heavy elements. *Geochem. Cosmochim. Acta* 71, 2170–2189. <https://doi.org/10.1016/j.gca.2007.02.004>.
- Schmidt, J.A., Jacob, D.J., Horowitz, H.M., Hu, L., Sherwen, T., Evans, M.J., Liang, Q., Suleiman, R.M., Oram, D.E., Le Breton, M., Percival, C.J., Wang, S., Dix, B., Volkamer, R., 2016. Modeling the observed tropospheric BrO background: importance of multiphase chemistry and implications for ozone, OH, and mercury. *J. Geophys. Res. Atmos.* 121, 11819–11835. <https://doi.org/10.1002/2015jd024229>.
- Schroeder, W.H., Anlauf, K.G., Barrie, L.A., Lu, J.Y., Steffen, A., Schneeberger, D.R., Berg, T., 1998. Arctic springtime depletion of mercury. *Nature* 394, 331–332. <https://doi.org/10.1038/28530>.
- Selin, N.E., Jacob, D.J., Park, R.J., Yantosca, R.M., Strode, S., Jaeglé, L., Jaffe, D., 2007. Chemical cycling and deposition of atmospheric mercury: global constraints from observations. *J. Geophys. Res.* 112 <https://doi.org/10.1029/2006jd007450>.
- Selin, N.E., Jacob, D.J., Yantosca, R.M., Strode, S., Jaegle, L., Sunderland, E.M., 2008. Global 3-D land-ocean-atmosphere model for mercury: present-day versus preindustrial cycles and anthropogenic enrichment factors for deposition. *Global Biogeochem. Cycles* 22, GB2011. <https://doi.org/10.1029/2008gb003282>.
- Shah, V., Jacob, D.J., Thackray, C.P., Wang, X., Sunderland, E.M., Dibble, T.S., Saiz-Lopez, A., Černušák, I., Kelló, V., Castro, P.J., Wu, R., Wang, C., 2021. Improved mechanistic model of the atmospheric redox chemistry of mercury. *Environ. Sci. Technol.* 55 (21), 14445–14456. <https://doi.org/10.1021/acs.est.1c03160>.
- Sherman, L.S., Blum, J.D., Johnson, K.P., Keeler, G.J., Barres, J.A., Douglas, T.A., 2010. Mass-independent fractionation of mercury isotopes in Arctic snow driven by sunlight. *Nat. Geosci.* 3, 173–177. <https://doi.org/10.1038/Ngeo758>.
- Si, M., McLagan, D.S., Mazot, A., Szponar, N., Bergquist, B., Lei, Y.D., Mitchell, C.P.J., Wania, F., 2020. Measurement of atmospheric mercury over volcanic and fumarolic regions on the North Island of New Zealand using passive air samplers. *ACS Earth Space Chem.* 4, 2435–2443. <https://doi.org/10.1021/acsearthspacechem.0c00274>.
- Sonke, J.E., 2011. A global model of mass independent mercury stable isotope fractionation. *Geochem. Cosmochim. Acta* 75, 4577–4590. <https://doi.org/10.1016/j.gca.2011.05.027>.
- Streets, D.G., Horowitz, H.M., Jacob, D.J., Lu, Z., Levin, L., Ter Schure, A.F.H., Sunderland, E.M., 2017. Total mercury released to the environment by human activities. *Environ. Sci. Technol.* 51, 5969–5977. <https://doi.org/10.1021/acs.est.7b00451>.
- Sun, G., Sommar, J., Feng, X., Lin, C.J., Ge, M., Wang, W., Yin, R., Fu, X., Shang, L., 2016a. Mass-dependent and -independent fractionation of mercury isotope during gas-phase oxidation of elemental mercury vapor by atomic Cl and Br. *Environ. Sci. Technol.* 50, 9232–9241. <https://doi.org/10.1021/acs.est.6b01668>.
- Sun, R., Streets, D.G., Horowitz, H.M., Amos, H.M., Liu, G., Perrot, V., Toutain, J.-P., Hintelmann, H., Sunderland, E.M., Sonke, J.E., 2016b. Historical (1850–2010) mercury stable isotope inventory from anthropogenic sources to the atmosphere. *Elementa Sci. Anthropocene* 4. <https://doi.org/10.12952/journal.elementa.000091>.
- Sun, R., Jiskra, M., Amos, H.M., Zhang, Y., Sunderland, E.M., Sonke, J.E., 2019. Modelling the mercury stable isotope distribution of Earth surface reservoirs: implications for global Hg cycling. *Geochem. Cosmochim. Acta* 246, 156–173. <https://doi.org/10.1016/j.gca.2018.11.036>.
- Sun, R., Yuan, J., Sonke, J.E., Zhang, Y., Zhang, T., Zheng, W., Chen, S., Meng, M., Chen, J., Liu, Y., Peng, X., Liu, C., 2020. Methylmercury produced in upper oceans accumulates in deep Mariana Trench fauna. *Nat. Commun.* 11, 3389. <https://doi.org/10.1038/s41467-020-17045-3>.
- Sun, R.Y., Sonke, J.E., Heimburger, L.E., Belkin, H.E., Liu, G.J., Shome, D., Cukrovsky, E., Lioussé, C., Pokrovsky, O.S., Streets, D.G., 2014. Mercury stable isotope signatures of world coal deposits and historical coal combustion emissions. *Environ. Sci. Technol.* 48, 7660–7668. <https://doi.org/10.1021/es501208a>.
- Wang, X., Yuan, W., Lin, C.J., Zhang, L., Zhang, H., Feng, X., 2019. Climate and vegetation as primary drivers for global mercury storage in surface soil. *Environ. Sci. Technol.* 53, 10665–10675. <https://doi.org/10.1021/acs.est.9b02386>.
- Wang, X., Luo, J., Yuan, W., Lin, C.-J., Wang, F., Liu, C., Wang, G., Feng, X., 2020. Global warming accelerates uptake of atmospheric mercury in regions experiencing glacier retreat. *Proc. Natl. Acad. Sci. Unit. States Am.* 117, 2049–2055. <https://doi.org/10.1073/pnas.1906930117>.
- Wesely, M.L., 1989. Parameterization of surface resistances to gaseous dry deposition in regional-scale numerical models. *Atmos. Environ.* 23, 1293–1304. [https://doi.org/10.1016/0004-6981\(89\)90153-4](https://doi.org/10.1016/0004-6981(89)90153-4).
- Wu, P., Zakem, E.J., Dutkiewicz, S., Zhang, Y., 2020. Biomagnification of methylmercury in a marine plankton ecosystem. *Environ. Sci. Technol.* 54, 5446–5455. <https://doi.org/10.1021/acs.est.9b06075>.
- Xu, H., Sonke, J.E., Guinot, B., Fu, X., Sun, R., Lanzanova, A., Caudaudap, F., Shen, Z., Cao, J., 2017. Seasonal and annual variations in atmospheric Hg and Pb isotopes in Xi'an, China. *Environ. Sci. Technol.* 51, 3759–3766. <https://doi.org/10.1021/acs.est.6b06145>.
- Yang, L., Sturgeon, R., 2009. Isotopic fractionation of mercury induced by reduction and ethylation. *Anal. Bioanal. Chem.* 393, 377–385. <https://doi.org/10.1007/s00216-008-2348-6>.
- Yang, S., Liu, Y., 2015. Nuclear volume effects in equilibrium stable isotope fractionations of mercury, thallium and lead. *Sci. Rep.* 5, 12626. <https://doi.org/10.1038/srep12626>.
- Yin, R.S., Feng, X.B., Meng, B., 2013. Stable mercury isotope variation in rice plants (*Oryza sativa* L.) from the Wanshan mercury mining district, SW China. *Environ. Sci. Technol.* 47, 2238–2245. <https://doi.org/10.1021/es304302a>.
- Young, E.D., Galy, A., Nagahara, H., 2002. Kinetic and equilibrium mass-dependent isotope fractionation laws in nature and their geochemical and cosmochemical significance. *Geochem. Cosmochim. Acta* 66, 1095–1104. [https://doi.org/10.1016/S0016-7037\(01\)00832-8](https://doi.org/10.1016/S0016-7037(01)00832-8).
- Yu, B., Fu, X., Yin, R., Zhang, H., Wang, X., Lin, C.J., Wu, C., Zhang, Y., He, N., Fu, P., Wang, Z., Shang, L., Sommar, J., Sonke, J.E., Maurice, L., Guinot, B., Feng, X., 2016. Isotopic composition of atmospheric mercury in China: new evidence for sources and transformation processes in air and in vegetation. *Environ. Sci. Technol.* 50, 9262–9269. <https://doi.org/10.1021/acs.est.6b01782>.
- Yu, B., Yang, L., Wang, L.L., Liu, H.W., Xiao, C.L., Liang, Y., Liu, Q., Yin, Y.G., Hu, L.G., Shi, J.B., Jiang, G.B., 2020. New evidence for atmospheric mercury transformations in the marine boundary layer from stable mercury isotopes. *Atmos. Chem. Phys.* 20, 9713–9723. <https://doi.org/10.5194/acp-20-9713-2020>.
- Yu, B., Yang, L., Liu, H., Yang, R., Fu, J., Wang, P., Li, Y., Xiao, C., Liang, Y., Hu, L., Zhang, Q., Yin, Y., Shi, J., Jiang, G., 2021. Katabatic wind and sea-ice dynamics drive isotopic variations of total gaseous mercury on the antarctic coast. *Environ. Sci. Technol.* 55, 6449–6458. <https://doi.org/10.1021/acs.est.0c07474>.
- Yuan, W., Sommar, J., Lin, C.J., Wang, X., Li, K., Liu, Y., Zhang, H., Lu, Z.Y., Wu, C.S., Feng, X.B., 2019. Stable isotope evidence shows re-emission of elemental mercury vapor occurring after reductive loss from foliage. *Environ. Sci. Technol.* 53, 651–660. <https://doi.org/10.1021/acs.est.8b04865>.
- Yuan, W., Wang, X., Lin, C.J., Wu, C., Zhang, L., Wang, B., Sommar, J., Lu, Z., Feng, X., 2020. Stable mercury isotope transition during post-depositional decomposition of biomass in a forest ecosystem over five centuries. *Environ. Sci. Technol.* <https://doi.org/10.1021/acs.est.0c00950>.
- Zhang, L., Wang, S., Wang, L., Wu, Y., Duan, L., Wu, Q., Wang, F., Yang, M., Yang, H., Hao, J., Liu, X., 2015. Updated emission inventories for speciated atmospheric mercury from anthropogenic sources in China. *Environ. Sci. Technol.* 49, 3185–3194. <https://doi.org/10.1021/es504840m>.
- Zhang, Y., Horowitz, H., Wang, J., Xie, Z., Kuss, J., Soerensen, A.L., 2019. A coupled global atmosphere-ocean model for air-sea exchange of mercury: insights into wet deposition and atmospheric redox chemistry. *Environ. Sci. Technol.* 53, 5052–5061. <https://doi.org/10.1021/acs.est.8b06205>.
- Zhang, Y., Song, Z., Huang, S., Zhang, P., Peng, Y., Wu, P., Gu, J., Dutkiewicz, S., Zhang, H., Wu, S., Wang, F., Chen, L., Wang, S., Li, P., 2021. Global health effects of future atmospheric mercury emissions. *Nat. Commun.* 12, 3035. <https://doi.org/10.1038/s41467-021-23391-7>.
- Zhang, Y.X., Jacob, D.J., Horowitz, H.M., Chen, L., Amos, H.M., Krabbenhoft, D.P., Slemr, F., St Louis, V.L., Sunderland, E.M., 2016. Observed decrease in atmospheric mercury explained by global decline in anthropogenic emissions. *Proc. Natl. Acad. Sci. U. S. A* 113, 526–531. <https://doi.org/10.1073/pnas.1516312113>.
- Zheng, W., Hintelmann, H., 2009. Mercury isotope fractionation during photoreduction in natural water is controlled by its Hg/DOC ratio. *Geochem. Cosmochim. Acta* 73, 6704–6715. <https://doi.org/10.1016/j.gca.2009.08.016>.
- Zheng, W., Hintelmann, H., 2010. Isotope fractionation of mercury during its photochemical reduction by low-molecular-weight organic compounds. *J. Geophys. Res. Atmos.* 114, 4246–4253. <https://doi.org/10.1021/jp9111348>.
- Zheng, W., Chandan, P., Steffen, A., Stuppel, G., De Vera, J., Mitchell, C.P.J., Wania, F., Bergquist, B.A., 2021. Mercury stable isotopes reveal the sources and transformations of atmospheric Hg in the high Arctic. *Appl. Geochem.* 131 <https://doi.org/10.1016/j.apgeochem.2021.105002>.
- Zhou, J., Obrist, D., Dastoor, A., Jiskra, M., Ryjkov, A., 2021. Vegetation uptake of mercury and impacts on global cycling. *Nat. Rev. Earth Environ.* 2, 269–284. <https://doi.org/10.1038/s43017-021-00146-y>.